HHS Public Access

Author manuscript

Immunity. Author manuscript; available in PMC 2026 May 21.

Published in final edited form as:

Immunity. 2026 May 12; 59(5): 1221–1236.e5. doi:10.1016/j.immuni.2026.04.003.

Age- and Tissue-dependent Diversity of Human Plasmacytoid Dendritic Cells Uncovers a Cycling Subset Dominant in Early Life and Cancer

Alina Ulezko Antonova[1], **Patrick Fernandes Rodrigues**[1], **Chelsea Mannie**[2], **Giorgia Ferrari**[3], **Horacio Carvajal Dominguez**[2], **Mattia Bugatti**[4], **William Vermi**[1,4], **Tong Wu**[1], **Marina Cella**[1,5], **Pirooz Eghtesady**[2,*], **Marco Colonna**[1,*,#]

[1]Department of Pathology and Immunology, Washington University of St. Louis School of Medicine, St. Louis, MO 63108, USA

[2]Department of Surgery, Division of Cardiothoracic Surgery, Washington University of St. Louis School of Medicine, St. Louis, MO 63108, USA

[3]Department of Immunology, H Lee Moffitt Cancer Center and Research Institute, Tampa, FL 33612, USA

[4]Department of Molecular and Translational Medicine, University of Brescia, Brescia 25125, Italy

[5]Present Address: Broad Institute of MIT and Harvard, Cambridge, MA 02142, USA

Summary

Plasmacytoid dendritic cells (pDCs) are innate sentinels that produce type I interferons (IFN-I) during infection. Here, we asked how developmental stage and tissue context shape human pDC transcriptional states. Single-cell RNA sequencing of pDCs from blood, thymus, lymph nodes, and tonsils across fetal, infant, and pediatric stages revealed tissue-enriched programs, including IFN-I–imprinted pDCs in thymus, NFκB-imprinted pDCs in tonsils, and resting pDCs in blood and lymph nodes. Across tissues, we identified a pDC subset characterized by prostaglandin D2 production and dopamine responsiveness, indicating a potential neuromodulatory axis. Cycling

*Co-correspondence: Pirooz Eghtesady (eghtesady670@wustl.edu) & Marco Colonna (mcolonna@wustl.edu).
#Lead Contact

Author contributions

A.U.A. and M.Co. conceptualized the project. A.U.A., G.F., P.F.R., and M.Ce. designed experiments. A.U.A. analyzed scRNA-seq data and made figures. A.U.A., G.F. and T.W. performed experiments and analyzed flow cytometry data. M.B. and W.V. performed immunohistochemistry stainings and analyzed the images. P.E. contributed to study design, preparation of the IRB and collection of the samples. A.U.A. and C.M. wrote the IRB with input from P.E. and M.Ce. C.M. and H.C.D. obtained consent and collected thymus, blood, and lymph node samples. A.U.A. wrote the initial draft with input from all the authors.

Declaration of interests

The authors declare no competing interests.

Declaration of generative AI and AI-assisted technologies in the manuscript preparation process

During the preparation of this work the authors used ChatGPT in order to shorten the length of the figure legends. After using this tool/service, the authors reviewed and edited the content as needed and take full responsibility for the content of the published article.

KEY RESOURCES TABLE

The key resources table is provided with this submission as a separate file.

pDCs were abundant in fetal and infant lymphoid tissues and declined with age, while remaining enriched in bone marrow throughout life. Blastic pDC neoplasm associated with enrichment of cycling, mutation-bearing pDCs in bone marrow, suggesting this niche serves as a reservoir for malignant pDCs. Thus, early in life, various lymphoid tissues can generate pDCs; this tissue-specific hematopoiesis may result in distinct cellular and functional outputs.

eTOC

Ulezko Antonova et al. examine plasmacytoid dendritic cells (pDCs) in lymphoid tissues from infancy to adulthood and identify a cycling population of pDCs in fetal and infant lymphoid organs, that is found only in the bone marrow in adults. pDCs in separate lymphoid tissues have distinct transcriptional profiles suggestive of specific functional outputs associated with tissue-specific hematopoiesis in early life.

Introduction

Plasmacytoid dendritic cells (pDCs) are immune cells specialized in rapid and robust production of type I interferons (IFN-I, i.e., IFN-α and IFN-β)[1-3]. They respond to exogenous and endogenous nucleic acids that reach Toll-Like Receptors (TLR) 7 and TLR9 in their endolysosomal compartment[4,5]. TLR7 and TLR9 initiate signaling cascades that lead to transcriptional activation of genes for IFN-I, proinflammatory cytokines and chemokines, co-stimulatory molecules like CD83, CD86, and CD40, and the chemokine receptor CCR7. In viral infections, IFN-I produced by pDCs establishes an antiviral state in surrounding cells, inhibiting viral replication and reducing viral spread[2,6]. However, dysregulated IFN-I production in response to endogenous nucleic acids is implicated in various autoimmune diseases, including Systemic Lupus Erythematosus[7-10], Multiple Sclerosis[11], and Systemic Sclerosis[12]. This dual nature of pDCs – protective in viral infections but potentially harmful in autoimmune conditions – underscores the importance of understanding their biology and regulation.

pDCs develop in the bone marrow (BM) from both the common lymphoid progenitor (CLP) and the common DC progenitor (CDP)[13-15]. Outside of the BM, pDCs are found in the blood, thymus, secondary lymphoid organs, such as spleen, lymph nodes, and tonsils, as well as non-lymphoid tissues such as liver and gut[1]. In humans, pDCs lack lineage (Lin) markers (CD3, CD19, CD14) and are uniquely identified by the cell surface receptor CLEC4C (also known as BDCA2). Additional cell surface markers, such as CD4, LILRB4 (also known as ILT3), CD123, and CD62L, are shared with other leukocytes[1]. In addition to pDCs, $Lin^{-}BDCA2^{+}$ leukocytes include a small population of $AXL^{+}SIGLEC1/6^{+}$ (AS)-DCs, also known as pDC-like cells[13,16-18] or transitional DCs (tDCs)[19]. AS-DCs are precursors of DC2s[16-18] and secrete inflammatory cytokines like IL-1β, IL-6, and TNF-α[20]. Most of the studies on human pDCs analyze cells isolated from peripheral blood. Thus, whether pDCs of different tissues exhibit some diversity remains unknown. Moreover, while it is established that pDC numbers decrease with age[21], the functional and phenotypic changes in pDCs across different age groups are largely unexplored.

Here, we used single-cell RNA sequencing (scRNA-seq) to profile Lin$^-$BDCA2$^+$ leukocytes, a population enriched in pDCs, from four human tissues with high pDC content: peripheral blood, thymus, perithymic lymph nodes (ptLNs), and tonsils. We focused on infants and children and also included adult blood, complementing our dataset with publicly available fetal and adult samples. Lin$^-$BDCA2$^+$ cells consisted largely of pDCs, a minor AS-DC subset, and a population of cycling pDCs. pDCs displayed distinct tissue-enriched states: an IFN-I–imprinted state enriched in thymus, an NF-κB–imprinted state prevalent in tonsils, and a resting state predominant in blood and ptLNs. These states were evolutionarily conserved. We also identified a PGD2-producing pDC subset present across tissues that expressed a dopamine-responsive inhibitory receptor. Cycling pDCs were abundant in fetal and infant lymphoid organs but consistently present in adult BM. In patients with pDC neoplasia, BM contained cycling pDCs with increased mutational burden, suggesting a potential leukemic reservoir. Together, these findings reveal tissue- and age-dependent pDC programs relevant to immunity, tolerance, and pDC-driven malignancy, with implications for antiviral, autoimmune, and cancer therapies.

Results

The human BDCA2$^+$ population contains pDCs, AS-DCs and cycling pDCs

To investigate the diversity of pDCs in the human immune system, we conducted 3' scRNA-seq on cells from blood samples (n=8) and lymphoid organs (n=15) with high pDC prevalence (Fig. 1A and S1A, B). These organs included the thymus (n=8), perithymic lymph nodes (ptLNs) (n=4), and tonsils (n=3) (Fig. 1A). Most of the samples originated from children (21 out of 23), with a male-to-female sample ratio of 12:11 (Fig. S1C, D). Six infants provided blood, thymus, and ptLN (Fig. S1E), enabling us to attenuate donor-specific differences. These donors underwent cardiac surgery with concomitant thymectomy. ptLNs were similarly harvested during the procedure, and blood was drawn preoperatively. Seven donors provided a single tissue (Fig. S1E): three infants provided thymi, three children undergoing elective tonsillectomy donated tonsils, and two adult donors contributed blood. Importantly, all specimens in our study were collected from living individuals, avoiding the high glucocorticoid levels typically present in organs from brain-dead donors, which are harmful to pDCs[22].

Following non-enzymatic tissue processing and magnetic enrichment, we sorted Lin$^-$(CD3/19/14)$^-$CD1c$^-$BDCA2$^+$ILT3$^+$CD123$^+$live cells, which are enriched in pDCs, resulting in a library of ~65,000 high-quality cells from a total of 16 unrelated donors (Fig. 1A, Fig. S1E). The dataset was processed with the *Seurat* pipeline[23] using the *Harmony* algorithm[24] to mitigate donor-specific differences. After removing a small cluster of contaminating T cells and a small cluster of cells unique to a single donor, the remaining cells were grouped into three major categories on a UMAP space: pDCs, marked by expression of *CLEC4C*, *GZMB*, and *LILRB4*[17]; AS-DCs, expressing *AXL* and *SIGLEC6*[17], and a small cluster of cycling pDCs marked by *MKI67* (Fig. 1B, C). To visualize the profile of each subset on a whole-transcriptome scale, we plotted the changes in gene expression on a 2-dimensional hexagonal radar chart (Fig. 1D). This approach revealed that AS-DCs exhibited a distinct and unique gene signature, including genes such as *AXL*, *SIGLEC6*, *HLA-DRB1,* and

S100A10[17], *IL1B*[20], *SPI1* and *KLF4*[16]. AS-DCs also expressed the tetraspanin protein *CD63*, which is involved in vesicular transport[25,26]; *VSIR* (V-Set Immunoregulatory receptor, also known as VISTA); *SEMA4A* (for semaphorin 4A), which drives Th2 responses[27]; *FGL2*, which is an inhibitory cytokine[28]; *COTL1* (for F-actin binding protein), and *VIM* (for vimentin), which may be involved in dendrite formation and motility[29] (Fig. 1D). Cycling pDCs had a distinct signature with a high number of differentially expressed genes (DEGs) (Fig. S1F) primarily encoding cycling machinery components (*MKI67, HMGB1*, and *TOP2A*), a component of the pre-B cell receptor (*IGLL1*)[30], and metabolic pathway genes such as *IDH2* and *LDHA* (Fig. 1D). Conversely, pDCs shared most distinguishing genes with either cycling pDCs or AS-DCs. For example, pDCs and cycling pDCs both expressed classical pDC markers such as *GZMB, IRF7, PTCRA, IL3RA*, and *JCHAIN*. The mRNA for the transcription factor *TCF4* was also equally enriched in both pDCs and cycling pDCs, suggesting a shared developmental pathway driven by TCF4[31] (Fig. 1D). Genes with common expression between pDCs and AS-DCs included the transcription factors *IRF4* and *KLF6*, as well as the LILR family gene *LILRA4* (Fig. 1D). Overall, these findings reveal that human $Lin^{-}CD1c^{-}$ $BDCA2^{+}ILT3^{+}CD123^{+}$ leukocytes, found across various tissues, consist of pDCs, AS-DCs, and cycling pDCs, each representing a transcriptionally distinct population.

Tissue-dependent abundance and programs of pDCs and AS-DCs

We examined the distribution of pDCs, AS-DCs and cycling pDCs across various tissues. pDCs constituted more than 85% of the sequenced cells across all tissues and donors, while AS-DCs and cycling pDCs were rare (1-10% and less than 1% per donor, respectively) (Fig. 1E, Fig. S1G-I). pDCs were evenly represented in the blood, thymus, and tonsil, and were moderately represented in the ptLN. In contrast, AS-DCs were primarily found in the blood and tonsil (Fig. 1F). Cycling pDCs were found predominantly in the thymus of all eight donors. Only two out of four donors exhibited cycling pDCs in their ptLN, and one donor showed a small number in their blood (Fig. S1G-I). Cycling pDCs were nearly absent in the tonsil (Fig. 1F). We conclude that pDCs are present in every organ analyzed, while AS-DCs are predominantly found in the blood and tonsils, and cycling pDCs are mainly found in the thymus of infants.

We next analyzed how pDC, AS-DC, and cycling pDC gene signatures vary across tissue microenvironments. Examining the top DEGs across all cell populations in each tissue, we found that tonsil pDCs exhibited the most distinct signature. This signature included genes such as *NFKBIA, CXCR4*, and *AREG*, along with *IER2*, the AP-1 transcription factors *JUN* and *FOSB*, and the activation markers *CD83* and *CCR7* (Fig. 1G). Pathway analysis revealed associations with TNFα signaling via NFκB, and hypoxia (Fig. 1H). Given that tonsils are commonly extracted due to inflammation or hypertrophy, this signature may reflect activation induced by pathogen exposure and inflammation. Thymic pDCs also displayed a distinct signature, characterized by several IFN-stimulated genes (ISG) such as *ISG15, ISG20, IFI44L, MX1, STAT1*, and *IFI27* (Fig. 1G, H). The ISG signature suggests that thymic pDCs are exposed to nucleic acids likely released by dead thymocytes in the medulla, triggering the secretion of IFN-I, which is known to activate pDCs through an

autocrine loop[32]. Thymic pDCs also expressed activation markers like *CCL3, CCL4, CD69, EGR1, CD83*, and *JUN* (Fig. 1G).

The gene signatures of blood and ptLN pDCs were similar to each other but distinct from those of the tonsil and thymus (Fig. 1G). These signatures lacked ISG and NFκB-related genes, suggesting a resting phenotype. Signature genes included *DACH1*, which binds SMAD4 and mediates TGFβ-mediated immune suppression[33]; *FCER1A*, the high-affinity receptor for IgE, which is elevated in circulating pDCs of children with persistent wheeze and asthma[34]; *ANTXR2*, the receptor for anthrax toxin; and the transcription factor *KLF12*, previously identified in pDCs and AS-DCs[19]. Blood pDCs expressed less lymphotoxin beta (*LTB*) than pDCs in other tissues (Fig. 1G). AS-DCs and cycling pDCs displayed tissue-specific gene signatures that were similar to those found in pDCs from the tonsil, thymus, blood, and ptLNs (Fig. 1G). This suggests shared responses to the tissue microenvironment. Accordingly, splitting the UMAP projection of pDCs, AS-DCs and cycling pDCs by tissue of origin confirmed distinct tissue patterns for the tonsil, thymus, and a combined pattern for blood and ptLNs (Fig. 1I).

Diverse pDC states show tissue-dependent abundance

Because pDCs are the most abundant subset, we focused on them to determine whether each tissue harbors a distinct pDC program or whether shared programs are present across tissues at different abundances. To maintain age homogeneity in our dataset, we reprocessed pDCs excluding the two adult samples. This analysis revealed ten distinct clusters (Fig. 2A, B). Cluster P was characterized by high expression of *PTGDS* (Prostaglandin D2 synthetase), *DRD4* (Dopamine Receptor D4), and *LCNL1* (Lipocalin-Like 1). This cluster was present in all tissues and represented 15% of all pDCs (Fig. 2A-C). Clusters N1-N3 were marked by high expression of NFκB-related molecules like *NFKBIA*, co-stimulatory ligands such as *CD83*, and the tissue modulator Amphiregulin (*AREG*) and were predominantly found in tonsils and partially in the thymus (Fig. 2A-C). Specifically, N3 was distinguished by transcripts for stress-response proteins (*DNAJB1, HSPA1A*), while N2 expressed chemokines *CCL3* and *CCL4*, and N1 lacked both groups of transcripts (Fig. 2B). Clusters I1-I2 were highly enriched in ISGs (Fig. 2B) and were prevalent in the thymus (Fig. 2C). Cluster I1 uniquely expressed *LY6E* and *IFI27*, while I2 had higher levels of *ENPP2* and *HIVEP3* (Fig. 2B). A small cluster (L) enriched in ptLN, thymus and blood expressed immunoglobulin light chains (*IGLC1-3*. Finally, a group of three neighboring clusters (R1-R3) encompassed resting pDCs, which were mostly present in blood and ptLN and shared the expression of the erythroid regulator *RHEX, PDE4B*, and *FAM160A1* (Fig. 2A-C). We further identified key genes that distinguished the major pDC clusters. *RHEX* marked resting pDCs, *AREG* distinguished activated tonsillar and thymic pDCs, and *ISG15* marked IFN-I-imprinted pDCs enriched in the thymus (Fig. 2D). Principal component analysis (PCA) of the same cells revealed that clusters N1-N3 were the most distinct, primarily present in tonsils and partly in the thymus (Fig. 2E). This observation suggests that tonsil pDCs receive NFκB activating signals from the tissue microenvironment. Furthermore, the PCA projection suggested that all tissues except the tonsils include resting pDCs. To validate this observation, we defined a resting pDC module using DEGs in blood pDCs versus tissue pDCs. Thymus and ptLN contained a clearly delineated group of cells expressing this

module, while the tonsils lacked such cells (Fig. 2F). This module features *CD52* (Table S1), which has been linked to diminished adhesion[35] and is consistent with a quiescent phenotype. Module-score enrichment analysis of a CD40L-activated pDC dataset[36] showed no enrichment of the resting pDC signature (Fig. 2G). A similar lack of resting-module expression was evident in pDCs from individuals with HIV[37] (Fig. 2H), corroborating that this module represents a *bona fide* resting state. Single-cell metabolomic analysis of scRNA-seq data using the scMetabolism package[38] revealed that resting pDCs were enriched in lipid biosynthesis and nicotinamide metabolism, while NFκB-imprinted pDCs displayed heightened metabolic activity, with significant enrichment in pathways such as glycolysis, pyruvate metabolism, oxidative phosphorylation, and amino acid degradation (Fig. S2A). Thus, distinct functional states of pDCs are associated with specific metabolic adaptations. We conclude that pDCs include functionally diverse *PTGDS*$^{+}$ pDCs, NFκB-imprinted pDCs, IFN-I-activated pDCs, *IGLC*$^{+}$ pDCs, and resting pDCs. These states are variably represented in blood, ptLNs, thymus and tonsils (Fig. 2I).

Human pDCs constitutively produce PGD2 and dopamine inhibits their activation

Since *PTGDS* is the gene that encodes for the enzyme that synthesizes PGD2, we sought to validate that *PTGDS*$^{+}$ pDCs produce PGD2. We isolated BDCA2^{+} cells – which mostly include pDCs and few AS-DCs (see Fig. 1B) — from peripheral blood mononuclear cells, stimulated them *in vitro* with TLR7 (Imiquimod) and TLR9 (CpG-A) agonists, and measured PGD2 in the culture supernatant (Fig. 2J). PGD2 production was elevated under steady-state conditions compared to media control, with minimal or no increase induced by Imiquimod or CpG-A (Fig. 2K). Since *PTGDS*$^{+}$ pDCs also express *DRD4* (Fig. 2B), an inhibitory dopamine receptor of the D2-like class, we examined whether dopamine impacts PGD2 release. Addition of dopamine to the culture medium did not affect basal PGD2 production (Fig. 2K). However, dopamine did reduce pDC production of IFN-β and IL-6 in response to Imiquimod and CpG-A (Fig. 2L-M). Moreover, it affected the expression of the activation markers CD86 and CCR7 induced by Imiquimod, and there was a trend toward reduced expression with CpG-A-induced activation (Fig. 2N). We conclude that *PTGDS*$^{+}$ pDCs produce PGD2 in the steady state, while DRD4 enables pDCs to respond to dopamine, which inhibits their activation by TLR7 and TLR9 agonists.

AS-DCs show diverse states with tissue-dependent abundance

Although less common than pDCs, our dataset contained a substantial number of AS-DCs, enabling a more in-depth analysis of AS-DCs in tissues. Re-clustering AS-DCs from all tissues revealed the presence of two main clusters projected on a UMAP, with signatures similar to those observed in resting and NFκB-imprinted pDCs (Fig. S3A). Cluster 1 resembled resting pDCs in blood and ptLNs, expressing genes like *RHEX, AFF3, PDE4B*, and *DACH1* (Fig. S3B). Cluster 2 was similar to NFκB-imprinted pDCs in tonsil, expressing genes like *NFKBIA, CXCR4, AREG* and *GPR183* (Fig. S3B). Resting AS-DCs predominated in blood and ptLNs, while activated AS-DCs were enriched in tonsils (Fig. S3C), indicating that the tonsil microenvironment favors activation. Resting and activated AS-DCs displayed different metabolic pathway gene expression patterns, similar to their corresponding pDC counterparts (Fig. S2B). In contrast to pDCs, IFN-I-imprinted (*ISG15*$^{+}$*IFI44L*$^{+}$), *IGLC*$^{+}$ and *PTGDS*$^{+}$ (*DRD4*$^{+}$*LCNL1*$^{+}$) AS-DCs did not form distinct

clusters but were present within resting and activated AS-DCs (Fig. S3D). Given that AS-DCs have been shown to be progenitors of DC2s[16], we investigated whether AS-DCs displayed features of maturing DC2s. We observed that NFκB-activated AS-DCs in tonsils upregulated MHCII antigen-presentation genes and *KLF4*, a transcription factor required for pDC-to-DC2 differentiation in mice[16]. At the same time, they downregulated *TCF4* and *ZEB2*, which are not expressed in DC2s (Fig. S3E). Together, these features suggest that NFκB-imprinted AS-DCs may participate directly in antigen presentation or represent a precursor state en route to DC2s.

Mouse tissues harbor conserved pDC, AS DC, and cycling pDC subsets

We investigated whether the three human Lin$^-$BDCA2$^+$ subsets found in representative tissues during early human life were also present in mouse tissues. To address this, we sorted all DCs [gated as Lin(CD3/CD19/NK1.1)$^-$MHCII$^+$CD11c$^+$] from six different organs of three 12-week-old C57BL/6 mice, and performed 3' scRNA-seq with HTO tagging. In addition, we processed a previously published dataset containing pDCs from the BM and the spleen[13]. The goal of generating this extensive mouse tissue dataset was to combine it with the human dataset. Since many genes in the mouse genome lack human orthologues and vice versa, we focused only on genes shared between the two species and present in both datasets, acknowledging that we may miss mouse-specific features. Using these orthologues, we reprocessed the mouse dataset. We then performed Canonical Correlation Analysis (CCA) for cross-species integration, resulting in a combined dataset represented in a single UMAP space (Fig. 3A-C). To ensure unbiased and cluster-agnostic cell type assignment, we employed a machine learning approach using Random Forest regression. We trained the model on the top 50 genes from the human pDC dataset, which could be used as a cell type classifier to fit various prediction datasets. We then applied this model to the integrated human and mouse dataset to verify if it accurately predicted the originally annotated cell types. The results confirmed that the mouse contained three subsets equivalent to the human *CLEC4C*$^+$ subsets (Fig. 3D): pDCs, marked by higher *TLR7* expression; AS-DCs, which expressed *CX3CR1*, were split into two subsets—resting and NFκB-imprinted (*CD83*$^+$); and *MKI67*+ cycling pDCs (Fig. 3D, E). AS-DCs also expressed *MKI67*, particularly in the murine thymus and BM, indicating the presence of proliferating subsets of AS-DCs in these two organs.

We then examined the tissue distribution of these three subsets in human and mouse tissues. Human pDCs were found in blood, ptLNs, thymus, and tonsils, while mouse pDCs were enriched in the BM and spleen (Fig. 3F, G and Fig. S4A, B). Human AS-DCs were mainly in blood and tonsils, whereas mouse AS-DCs were abundant in the spleen and thymus. Cycling pDCs were primarily in the human thymus and abundant in mouse thymus and BM (Fig. 3G, and Fig. S4A, B). Transcriptionally, there were notable differences between the two species (Fig. 3H and Fig. S4C). To determine if the functional states identified in human pDCs were also present in mice, we conducted the same Random Forest training process specifically for pDCs (see Fig. 2). All mouse organs exhibited a resting state, while the NFκB state was particularly prominent in the spleen and mesenteric lymph nodes (Fig. S4D, E). The *PTGDS*$^+$*DRD4*$^+$ state was entirely absent in mouse (Fig. S4D-E), suggesting it is a module unique to humans.

Cycling pDCs are found in neonatal thymus and persist in BM throughout life

The finding that cycling pDCs are present in human infant tissues and conserved in mice was surprising given that pDC proliferation is thought to be restricted to the BM[39]. To functionally validate the scRNA-seq data indicating the presence of cycling pDCs in the thymus of infants, we stained infant thymocytes for nuclear Ki-67. pDCs expressed Ki-67 as did double negative (DN) thymocytes, which are known to proliferate during T cell development[40,41] (Fig. 4A, B). In contrast, Ki-67 was not expressed in pDCs from infant blood (Fig. 4C, D) or pDCs from adult blood (Fig. 4E, F). We confirmed the presence of Ki-67$^+$ pDCs by immunohistochemistry of thymic sections and cytology of thymic cell suspensions (Fig. 4G).

To investigate cycling pDCs in adults we examined the Cross-Tissue Immune Cell Atlas (CTICA)[42], which encompasses 10 distinct adult immune tissues. To capture all pDC-related subsets, we extracted cells annotated as “pDC” in the dataset. Reprocessing of these data confirmed the presence of pDCs, AS-DCs and cycling pDCs as three distinct populations (Fig. S5A, B). Tissue distribution analysis showed that pDCs and AS-DCs were present in various tissues; cycling pDCs were mainly found in the BM and in trace amounts in the spleen (Fig. S5C). Although adult thymi were absent from this dataset, reanalysis of an external atlas[43] showed that cycling pDCs persisted in adult thymus, but at decreasing abundance with age (Fig. 4H). We cross-compared this finding with an independent BM dataset[44], which corroborated a high abundance of cycling pDCs (Fig. S5D-F). We validated the presence of Ki-67$^+$ pDCs by immunohistochemical stainings of adult BM samples aligning with the scRNA-seq results (Fig. S5G). Conversely, analysis of an independent spleen dataset[45] failed to detect cycling pDCs (Fig. S5H, I). We conclude that the BM harbors readily detectable *bona fide* cycling pDCs throughout life.

Cycling pDCs are enriched in fetal lymphoid organs

Because cycling pDCs were abundant in infant tissues, yet scarce in tonsils of older children and undetectable in adult blood (Fig. 5A), we investigated whether cycling pDCs are broadly present across fetal organs. To test this hypothesis, we analyzed a recently published scRNA-seq atlas of human prenatal organs[46]. We identified a *CLEC4C*$^+$ cell cluster, annotated as cycling pDCs (Fig. 5B), which expressed the same markers as the cycling pDCs we found in the thymus, including *MKI67* and *IGLL1* (Fig. 5C). We next examined which fetal organs contained cycling pDCs. By splitting this re-processed dataset of human prenatal organs, we noted that cycling pDCs were abundant in the fetal BM, liver, spleen, and yolk sac, but not in non-lymphoid tissues such as the kidney or the gut wall (Fig. 5D). Immunohistochemical analysis corroborated the presence of *KI67*$^+$ pDCs in fetal thymi and lymph nodes (Fig 5E-F). These results aligned with our observation that cycling pDCs are present in early postnatal lymphoid organs such as the thymus and ptLN. Of note, fetal lymphoid organs also contained cycling AS-DCs.

To confirm that the cycling pDCs identified in the fetal atlas correspond to the same subset found in our thymic data, we integrated our dataset of pDCs, AS-DCs, and cycling pDCs from infants (blood, thymus, ptLNs), young children (tonsils), and adults (blood) with similar cell populations identified in the fetal atlas (Fig. 5G-H). This showed that

cycling pDCs were readily detectable in fetuses and infants but became scarce in children and adults (Fig. 5I). Conversely, AS-DCs increased with age. We then examined whether their profiles overlapped in the UMAPs before and after birth. This integration showed that cycling pDCs were the only *CLEC4C*$^{+}$ subset that remained consistent in both fetal and postnatal UMAPs, as their clusters occupied the same location. In contrast, pDC and AS-DC clusters shifted locations in the UMAPs after birth (Fig. 5H). This modest shift in the transcriptional programs of pDCs and AS-DCs after birth was partially driven by a decrease in lymphoid marker expression and the emergence of *PTGDS, DRD4* and *LCNL1* (Fig. 5J). In conclusion, these findings suggest that cycling pDCs are present in the primary and secondary lymphoid organs of fetuses and infants. As individuals age, cycling pDCs are mainly detected in the BM.

Cycling pDCs encompass pDC and DC2 precursors

We sought to determine whether cycling pDCs represent progenitors of pDCs. CellRankbased pseudotime and k-nearest-neighbor trajectory mapping[47] placed cycling pDCs upstream of pDCs in datasets of BM[44] (Fig. 6A), fetal tissues[46] (Fig. 6B), and thymus[43] (Fig. 6C-D), with a smaller branch toward DC2s. To complement atlas-level analyses, we re-analyzed a scRNA-seq dataset of DCs differentiated from BM CD34^{+} progenitors[48] (Fig. S6A). Reclustering identified a proliferating *MKI67*$^{+}$ *IGLL1*$^{+}$ *IDH2*$^{+}$ population corresponding to cycling pDCs that occupied a position between pDCs and DC2s (Fig. 6E-F), and CellRank trajectories again suggested predominant differentiation into pDCs with a smaller flux toward DC2s through an *IGLL1*$^{-}$ intermediate (Fig. 6F, G).

To test precursor potential experimentally, we isolated CD4^{Low} thymic pDCs, which expressed higher Ki-67 and CD34 than CD4^{High} pDCs (Fig. S6B-E). Notably, CD4^{Low} pDCs were a minority within BDCA2^{+} cells (Fig. S6F) and showed expression of receptors for FLT3L, SCF, GM-CSF, and IL-3 (Fig. S6G). Because sorting of this population resulted in very low cell numbers (1,000-5,000 cells, depending on the donor), we thought to maximize their proliferation potential with a cytokine cocktail that engaged most cytokine receptors expressed. Indeed, when sorted and cultured with IL-3, SCF, GM-CSF, and FLT3L, CD4^{Low} pDCs expanded more robustly than CD4^{High} pDCs (Fig. S6H-K), incorporated more BrdU (Fig. S6L-O), and generated CD1c^{+}CD11c^{+} DC2-like cells (Fig. S6P-S). Virtually no CD1c^{+}CD11c^{+} cells developed in the presence of IL-3 alone from CD4^{High} pDCs (Fig. S6R). The bias toward DC2s was likely driven by the culture conditions, consistent with the fact that GM-CSF is known to inhibit pDC differentiation[49,68]. Conditions that support pDC differentiation and survival *in vitro* remain to be established. Together, these transcriptomic and functional data suggest that cycling pDCs harbor proliferative precursors capable of giving rise to both pDCs and DC2s, with lineage outcome shaped by cytokine tissue availability and context.

Cycling pDCs coincide with pDC precursors found in other datasets

To assess whether thymic cycling pDCs beared any similarity to other known pDC and/or DC2 precursors, we cross-compared their signature to those in other databases using the Coresh tool[51]. One of the hit databases was a study by Lavaert *et al.*[52], which screened neonatal thymus for non-T cell progenitors[52]. In this study, computational predictions

suggested that GMP_IRF8^{hi} cells give rise to pDCs, although experimental validation was lacking. A later study demonstrated that this precursor has exclusive pDC potential[53]. To assess similarity of GMP_IRF8^{hi} to cycling pDCs, we integrated our thymic dataset with that of Lavaert *et al.* using CCA. We found that GMP_IRF8^{hi} cells corresponded to cycling pDCs in a UMAP projection (Fig. 6H)

We also examined a dataset of DCs that differentiated *in vivo* from human hematopoietic precursors implanted in a mouse skin model[54]. In these settings, matrigel skin plugs containing progenitors and feeder cells gave rise to various DCs, among which we noted pDCs expressing *MKI67, IGLL1, IGLC2*, and *TCF4* (Fig. 6I), which corresponded to cycling pDCs in our database. Overall, these data suggest that cycling pDCs represent a proliferating precursor stage that may differentiate into pDCs or DC2s depending on microenvironmetal cues.

Cycling pDCs are expanded and hypermutated in a pDC tumor

We explored the involvement of cycling pDCs in disease, specifically focusing on Blastic Plasmacytoid Dendritic Cell Neoplasm (BPDCN)[55]. BPDCN is an aggressive form of skintropic pDC leukemia that primarily affects males in their 60s. This disease originates from premalignant BM cells in most cases bearing *TET2* mutations, which migrate to the skin and become overly malignant due to additional mutations induced by ultraviolet (UV) light exposure. These leukemic cells can remain confined to the skin or spread back to the BM. A recent study by Griffin *et al.* reported a scRNA-seq dataset from BM samples of BPDCN patients with or without BM involvement, defining a BM BPDCN signature by contrasting the two groups[56]. We compared this BM BPDCN signature with the transcriptional profiles of pDCs, AS-DCs, and cycling pDCs identified in our study. The BM BPDCN signature was enriched in cycling pDCs (Fig. 7A), suggesting that this subset, more than pDCs or AS-DCs, might be involved in BPDCN. Interestingly, among the 29 genes shared by BM BPDCN and cycling pDCs, only nine were linked to cell proliferation (Fig. S7A). This suggests that the connection between cycling pDCs and BPDCN malignant cells extends beyond the cell cycle alone, as the signature enrichment in cycling pDCs persists even when cell cycle–related genes are removed (Fig. 7B). Immunohistochemical analysis of BPDCN specimens confirmed that high expression of Isocitrate Dehydrogenase 2 (IDH2) on leukemic cells (Fig. S7C, D), a marker of cycling pDCs (see Fig. 1D) that is frequently mutated in BPDCN[57].

Next, we reprocessed the BPDCN dataset to investigate the presence of cycling pDCs in the BM of patients with or without BM involvement (Fig. 7B). Cells identified as “pDC” by Griffin *et al.* in the BPDCN study[56] using a Random Forest Machine Learning approach appeared as three distinct subsets in our UMAP: one as a standalone population, another as a small subset close to B cells, and a third subset clustering with DCs (Fig. 7B). We next mapped the DNA mutations onto the single cells in this UMAP using eXpressed Variant Sequencing (XV-Seq) information collected in parallel with scRNA-seq. We found that most cells with at least one mutation corresponded to these three groups of pDCs (Fig. 7C). When we divided the UMAP containing the mutation data by patients with and without BM involvement, we noted that the cells carrying mutations predominantly came from patients

with BM involvement (Fig. 7D, E and Fig. S7E). This supports the hypothesis that the BM pDC populations included most of the BPDCN leukemic cells[56].

To determine which subset of cells classified as “pDC” in the study by Griffin *et al.* corresponded to the subsets identified in our study, we reprocessed this cluster only. By transferring our signature scores to the reprocessed dataset (Fig. S7F-H) we identified three main clusters: one expressing the canonical genes of AS-DCs (1); one corresponding to cycling pDCs (2); and a third one resembling canonical pDCs (3) (Fig. 7F, G and S7F-H). The pDC cluster also included a small subset of cells that expressed *IGLC2/3*. Next, we quantified the abundance and the mutations in each cluster. Patients with BM involvement exhibited parallel expansion of cycling pDCs and pDCs (Fig. 7H). However, cycling pDCs included cells with most mutations (3-5 mutations/cell) as compared to pDCs and AS-DCs (Fig. 7I). We conclude that cycling pDCs in BPDCN are a major reservoir of mutated cancer cells. Although no BPDCN samples from skin were available, we mined a database of BPDCN from blood[17], a route that mutated cells must use to travel from the BM to the skin and vice versa. Projection of the blood BPDCN signature onto our primary cells showed an overlap with cycling pDCs – a relationship that, again, extended beyond the cell cycle (Fig. 7J and Fig. S7I, J). We conclude that cycling pDCs are highly mutated and expanded in the BM of BPDCN patients who have BM involvement, potentially contributing to the proliferative pool of BPDCN blasts.

Discussion

Our comprehensive scRNA-seq profiling of pDCs from human lymphoid tissues and blood across developmental stages uncovers distinct pDC states with tissue-skewed representation. pDCs in the blood and lymph nodes are in a resting state, while those in the thymus of infants and children are IFN-I-imprinted. In the tonsils of children, pDCs show an NFκB-imprinted state. In the tonsils, pDCs are most likely indirectly activated by cytokines released in response to microbial stimuli, as result of ongoing inflammation[58]. In contrast, in the thymus pDCs might be directly activated by nucleic acids released from apoptotic thymocytes via the TLR9 or cGAS-Sting pathway[36,59], triggering secretion of IFN-I, which further activate pDCs through an autocrine loop[32]. Due to the different source and type of stimulation, pDCs may either adopt an IFN-I or a NFκB signature[60,61]. Accordingly, previous and recent studies show that pDC stimulation with the inflammatory cytokine TNF-α disable pDC capacity to produce IFN-I[36,62]. In thymus, pDCs may also be activated by IFN-I which is produced by thymic epithelial cells to support the development of a diverse and tolerant TCR repertoire[63].

Beyond these states, we identify a pDC state across all tissues characterized by PGD_2 production, expression of the dopamine receptor DRD4, and dopamine responsiveness, which we functionally validate. This state is undetected in any mouse datasets we examined, though it may arise in activated or disease-associated murine pDCs for which single-cell data are lacking. PGD_2 is a lipid mediator that recruits and activates cells involved in allergic inflammation through CRTH2[64], such as eosinophils and group 2 innate lymphoid cells. Thus, PGD_2 production, along with the previously reported expression of the high-affinity IgE receptor, *FCER1A*, suggests a potential role for pDCs in type 2 immune responses such

as asthma, allergic rhinitis, and other allergic diseases[65]. Exposure of pDCs to dopamine reduces pDC activation and cytokine secretion in response to TLR7 and TLR9 agonists. These data reveal a potential mechanism of pDC regulation, seemingly unique to human, in line with a previous report showing that natural amines inhibit human pDC production of IFN-α[66]. Since dopamine-releasing neurons are enriched in perivascular regions where pDCs are more abundant[67], this may be a key area where dopamine-mediated pDC regulation occurs.

Due to their phenotypic similarities, we isolated pDCs along with the rarer AS-DCs and cycling pDCs, which we also characterize using scRNA-seq. While AS-DCs are functionally distinct from pDCs, we observe that they exhibit similar resting and activation states, suggesting that AS-DCs may respond to tissue microenvironments in ways comparable to pDCs. An intriguing finding relates to the age-dependent dynamics of cycling pDCs. In fetuses and infants, these cells are broadly distributed across several primary and secondary lymphoid organs, including the thymus, spleen, liver, and lymph nodes, as well as in the yolk sac. However, as individuals age, the presence of proliferating pDCs is mainly detectable in the BM, which is the primary site of pDC development in adults[13-15]. This shift likely reflects the decline in prenatal and perinatal hematopoiesis in lymphoid organs over time. Bioinformatic analyses of cycling pDCs in human single-cell atlases and in $CD34^+$ progenitor-derived cultures suggest that they include progenitors with potential to generate both pDCs and DC2s. However, when thymic cycling pDCs are cultured in vitro under a cytokine cocktail containing GM-CSF, SCF, IL-3 and FLT3L, they yield mostly DC2s, consistent with previous and recent reports of blood pDCs adopting a DC2 fate[36]. Because GM-CSF suppresses pDC differentiation[49,68], these conditions likely bias lineage output toward DC2s. Therefore, culture conditions that support pDC differentiation and survival from thymic $CD4^{Low}CD34^{+/-}$ cycling pDCs remain to be defined.

Beyond their developmental role, we find a notable population of cycling pDCs in the BM of patients with BPDCN, an aggressive pDC malignancy that arises from premalignant pDCs in the skin due to UV-induced mutations. In patients in which leukemic cells spread to the BM, cycling pDCs show a high frequency of DNA mutations. Moreover all leukemic cells express *IDH2*, a marker of cycling pDCs. Thus, these cells may contribute significantly to the pool of mutated leukemia cells. Given that other aggressive forms of skin leukemia are also linked to pDCs[50], the identification of cycling pDCs opens the door to detailed characterization of their phenotypic and functional profiles, which may help in identifying therapeutic targets for treating these malignancies.

STAR Methods

RESOURCE AVAILABILITY

Lead contacts: Further information and requests for resources and reagents should be directed to and will be fulfilled by the lead contact Dr. Marco Colonna (mcolonna@wustl.edu).

Materials availability: This study did not generate new unique reagents.

Data and code availability: Single-cell RNA-seq data have been deposited at GEO (accession number GSE273852) and will be publicly available as of the date of publication. Accession numbers will be listed in the key resources table. All original code has been deposited at GitHub and will be publicly available as of the date of publication. The GitHub link will be listed in the key resources table. Any additional information required to reanalyze the data reported in this paper is available from the lead contact upon request.

EXPERIMENTAL MODEL AND STUDY PARTICIPANT DETAILS

Human sample collection: Peripheral blood samples from adults were collected from discarded leukoreduction system chambers from apheresis procedures. Mononuclear cells were obtained via a Ficoll density gradient centrifugation, and the cells remained in 5 mL of MACS buffer overnight before sorting and preparing the libraries for scRNA-seq. For enrichment of pDCs, cells were positively selected with anti-BDCA4 magnetic beads prior to flow cytometry assisted cell sorting (FACS).

Tonsils were obtained from elective tonsillectomies performed at the Children's Hospital in St. Louis, where they were provided as surgical waste with no identifiers attached. Tonsillar tissue was mechanically disrupted, passed through a 0.059-inch opening sieve and filtered extensively through 70-μm cell strainers. To get rid of the dominant B and T cell populations and thus enrich the pDCs, single cell suspensions were negatively depleted of T and B cells using anti-CD3 and anti-CD19 magnetic beads prior to FACS. Thymuses, pTLNs and neonatal blood were obtained from neonates undergoing cardiac surgeries, as they typically have their thymus and adjacent thymic bed removed because it disrupts the view of the heart during surgery. The samples collected for sequencing had no known genetic anomalies. The fragment of the thymus and the thymic bed, containing several ptLNs, that are removed are typically discarded as medical waste. Additionally, blood can be collected at the time of surgery before the patient goes on cardiopulmonary bypass. The volume of blood collected was determined by the patient's age and weight. Upon the family's permission to the donation of the infant's thymus, pTLNs and/or blood (IRB ID # 202009010), tissues were processed in the following way: 1) blood was processed in the same manner as adult blood (see first paragraph of this section); 2) thymus was first cut into 2-3 pieces and left overnight in 5mL of MACS buffer. The next day, it was mechanically minced and filtered extensively through 70-μm cell strainers. To positively enrich pDCs, thymocytes were positively selected with anti-BDCA4 magnetic beads prior to FACS; 3) pTLNs were first left overnight in 5mL of MACS buffer. The next day, they were mechanically minced and filtered extensively through 70-μm cell strainers prior to FACS. The excision of ptLNs from the rest of the thymic bed was done by the operating surgeons. To further confirm the absence of thymic tissue in the excised lymph nodes, the lymph nodes were visualized under a light microscope and only used if a clear capsule surrounding it was visible, without freely floating lymphocytes, as observed in thymic tissue.

The sex and age range of the participants is detailed in Fig. S1. The ancestry, race, ethnicity and socioeconomic status of the participants could not be recovered due to the strict guidelines of the IRB.

METHOD DETAILS

FACS isolation of pDCs: Fresh, magnetically enriched cells (except for ptLNs, which were not enriched) were washed in MACS buffer and counted to analyze cell viability. Next, cells were resuspended in a cell staining buffer and stained with antibodies for the identification of pDCs. All samples were stained with the same antibodies. Specifically, samples were stained with anti-CD3 (PerCP-Cy5.5, Biolegend), anti-CD19 (PerCP-Cy5.5, Biolegend), and anti-CD14 (PerCP-Cy5.5, Biolegend) to exclude T cells, B cells and monocytes, respectively; anti-CD1c (BV510, Biolegend) to exclude mature DC2s; and anti-ILT3 (PE-Cy7, Biolegend), anti-CD123 (PE, Biolegend) and anti-BDCA2 (FITC, Millteny) to positively identify pDCs. We performed purity checks and achieved a very high purity (>98%). The cells were sorted using flow cytometry on BD FACS Aria II and cells were analyzed via flow cytometry on a BD FACSymphony A3 instrument. Data were analyzed with the FlowJo software v10.8.1 (TreeStar).

Stimulation of pDCs with CpGA and Imiquimod with or without dopamine: pDCs were plated at 5×10^4 cells in 200 μL of complete culture medium supplemented with IL-3 (Peprotech, 10ng/ml). Dopamine (Sigma, 10 μM) was added to designated wells one hour prior to stimulation. Cells were then stimulated overnight with CpGA (Invivogen) or Imiquimod (Invivogen) in the presence or absence of dopamine. Following stimulation, cells were collected for analysis of phenotype or downstream assays. For pDC characterization and purity assessment, 50 μL was sampled from each well, and cells were stained in 100 μL buffer with anti-BDCA2 (FITC, Millteny), and anti-ILT3 (PE-Cy7, Biolegend), anti-CD86 (PE, Biolegend), anti-CCR7 (APC-Cy7, Biolegend). Supernatants were frozen and analyzed by ELISA for IFNβ(PBL), Prostaglandin D2 (MyBiosource), and inflammatory citokine (Human Inflammatory Cytokine CBA assay, BD) content.

Sorting of $CD4^{Low}CD34^{+/-}$ cycling pDCs from thymus: pDCs were sorted as Live, Singlets, $Lin^-(CD3/19/14)^-CD1c^-BDCA2^+ILT3^+CD123^+$, $CD4^{Low}$, $CD34^{+/-}$ or $CD4^{High}$. Three out of the six patients collected for these assays had Trisomy 21. The same number of cells from each gate was cultured in a 96 well U bottom plate in the presence of 4% FLT3L supernatant, SCF (Peprotech, 100ng/ml), IL-3 (Peprotech, 100ng/ml) and GM-CSF (Peprotech, 100ng/ml). The input number of cells was based on cell recovery from the $CD4^{Low}/CD34^{+/-}$ fraction. $CD4^{High}$ pDCs were additionally cultured in IL-3 alone (100ng/ml), because many more cells were recovered from this gate and served as a negative control. Cells were analyzed after 5-7 day of culture. For BrdU incorporation and detection, we incubated cells with 10 uM BrdU overnight followed by staining with anti-BrdU-PE (Biolegend) using the BD Pharmingen BrdU Flow kit, as instructed by the manufacturer.

Immune cell harvest from mouse tissues: Dendritic cells from the spleen, lymph nodes (LNs), thymus, and lungs were obtained by enzymatic digestion in Collagenase D (1 mg/mL) for 30 min at 37°C. Red blood cell lysis of bone marrow, spleen, and lung suspensions was performed using 1× Red Blood Cell Lysis Buffer (BioLegend). All samples were passed through a 70-μm cell strainer prior to downstream processing. For cell sorting, a BD FACSAria II was used, and cells were collected in phosphate-buffered saline

(PBS) supplemented with 0.5% bovine serum albumin and 2.5 mM EDTA. Cell purity was confirmed to be ≥95% by post-sort analysis.

Human 3' scRNA-seq library preparation: Freshly isolated cells from paired tissues were subjected to a Cell Hashing protocol before proceeding to scRNA-seq. Cell hashing was performed before sorting following manufacturer's instructions (Cell hashing and Single Cell Proteogenomics Protocol Using TotalSeqB™ Antibodies; BioLegend). Briefly, prior to sorting, cells from each sample were labelled with a unique hashtag antibody. Following the sort, cells were washed 2 times (the first time in media and the second time in 0.04% BSA), and finally resuspended in an appropriate volume of PBS+0.04% BSA to obtain a final cell concentration >1000 cells/μl, suitable for scRNA-seq, according to the 10X platform. Individual sorted samples were brought individually to the McDonnell Genome Institute (MGI) at Washington University in St. Louis and mixed immediately prior to being loaded on a 10X Genomics Chromium Single Cell Controller. For library preparation, the 10X Genomics Next GEM Single Cell 3' Reagents Kit was used. This process utilized the Chromium Next GEM Single Cell 3′ Kit v3.1 (16 rxns), Chromium Next GEM Chip G Single Cell Kit (48 rxns), and Dual Index Kit TT Set A (96 rxns). In brief, up to 23,000 cells were partitioned into nanoliter Gel-bead-in-Emulsions (GEMs) droplets, each containing retro-transcriptase reaction mix. Single-cell cDNA received a unique 12-nucleotide barcode and unique molecular identifier (UMI). Subsequently, GEM cDNA underwent 11 cycles of amplification before purification using SPRIselect beads. The generation of geneexpression (GEX) and hashtag-oligo (HTO) libraries followed the recommendations provided in the 10x Genomics Chromium Single Cell 3′ Reagent Kits User Guide (v3.1 Chemistry Dual Index), with modifications to PCR cycles based on the calculated cDNA concentration. The concentration of each library was determined using qPCR with the KAPA library Quantification Kit following the manufacturer's protocol (KAPA Biosystems/Roche). The sequencing of normalized cDNA libraries was performed on a NovaSeq6000 S4 Flow Cell using the XP workflow and a 28×10×10×150 sequencing recipe as per the manufacturer's protocol (Illumina). A median sequencing depth of 50,000 and 5,000 reads per cell was targeted for the GEX and HTO library, respectively.

Mouse 3' scRNA-seq library preparation: Dendritic cells were isolated from skin-draining lymph nodes (sLN), mesenteric lymph nodes (mLN), spleen, thymus, and lung of three C57BL/6 mice. Tissues were processed into single-cell suspensions and enriched for $CD11C^+$ cells. cDC1s ($CD19^{™}CD3^{™}BST2^{™}SIGLECH^{™}CD11C^+MHC\text{-}II^+XCR1^+CD11B^{™}$), cDC2s ($CD19^{™}CD3^{™}BST2^{™}SIGLECH^{™}CD11C^+MHC\text{-}II^+XCR1^{™}CD11B^+$), and pDCs ($CD19^{™}CD3^{™}BST2^+SIGLECH^+$) subsets were sort-purified from all tissues.

Prior to sorting, each tissue suspension was labeled with a unique TotalSeq-A Hashtag antibody (HTO). For Sample 1, mouse 1 was labeled with HTO-1 (Skin), HTO-4 (sLN), and HTO-7 (mLN); mouse 2 with HTO-2 (Skin), HTO-5 (sLN), and HTO-8 (mLN); and mouse 3 with HTO-3 (Skin), HTO-6 (sLN), and HTO-9 (mLN). For Sample 2, the same mouse-specific HTO assignments were used, such that spleen samples were labeled with HTO-1, HTO-2, and HTO-3, thymus with HTO-4, HTO-8, and HTO-9, and lung with

HTO-5, HTO-6, and HTO-7 across the three mice. Following sort-purification, cells from each tissue were pooled per sample and resuspended in PBS containing 0.04% BSA at approximately 1,000 cells/μL, and subsequently loaded into a 10x Genomics Chromium Single Cell Controller at the McDonnell Genome Institute (Washington University in St. Louis).

Single-cell libraries were prepared using the Chromium Next GEM Single Cell 3′ Kit v3.1, Chromium Next GEM Chip G Single Cell Kit, and Dual Index Kit TT Set A. Approximately 20,000–23,000 cells were partitioned into Gel Bead-in-Emulsions (GEMs), enabling barcoded cDNA synthesis with unique molecular identifiers (UMIs), followed by cDNA amplification (11 cycles) and size-selection using SPRIselect beads. Gene expression (GEX) and Hashtag-oligo (HTO) libraries were generated according to the manufacturer's protocol (10x Genomics Single Cell 3′ Reagent Kits v3.1, Dual Index). Libraries were quantified using the KAPA Library Quantification Kit (Roche). Sequencing was performed on an Illumina NovaSeq 6000 S4 flow cell using a 28×10×10×150 read configuration. Target sequencing depth was ~50,000 reads per cell for GEX libraries and ~5,000 reads per cell for HTO libraries.

scRNA-seq downstream analysis: scRNA-seq downstream analyses were performed using the Seurat software package version 4.0 for R (http://satijalab.org/seurat/). For barcoded samples, *Seurat*'s *HTODemux* function was used as described previously (https://satijalab.org/seurat/articles/hashing_vignette). After removing unwanted cells and genes from the dataset, raw UMIs in each cell were both scaled and normalized via the *SCTransform* function. To improve downstream dimensionality reduction and clustering, we regressed out unwanted source of variation arising from the percentage of mitochondrial genes. Then, highly variable genes were identified and selected for PCA reduction of high-dimensional data. Cells in this reduced space were harmonized to adjust for batch effects coming from multiple donors using the *Harmony* tool implemented in *Seurat*. These low dimensional corrected *Harmony* embeddings were used for downstream analyses. Graph-based clustering analysis was performed on the reduced data with *Seurat*. The resolution in the *FindClusters* function from *Seurat* was set at values between 0.3 and 0.7, and the clustering results were shown in a computed UMAP plot (dims = 1:20). Different cell types were grouped based on top markers. For each cluster, DEGs were generated relative to cells in all other clusters via the *FindMarkers* function. Genes were considered to be DEGs if they were present in at least 10% of cells and they were higher than 2.5 log Fold Change (FC) in one cluster as compared to all other clusters. Violin plots were generated using the *VlnPlot* function in *Seurat*. Heatmaps of individual cells were plotted using the *DoHeatmap* function from Seurat by selecting the top 10 DEGs in each cluster. Genes that were discarded during the *SCTransform* process were not represented in those heatmaps. Heatmaps of average gene expression were generated by using the *AverageExpression* function from *Seurat* and then plotted using the *DoHeatmap* function.

The hexagonal plot to display cluster specific and shared genes among the three cell subsets contained within the BDCA2^{+} gate was performed as described by the original authors of the package (https://zouter.github.io/triwise/vignette.html#plotting-gene-expression-of-three-conditions) with slight modifications. pDCs, AS-DCs and cycling pDCs were subsetted to

1000 cells/group and the *averageExpression* function was run to generate a pseudobulked count matrix. Then, the *transformBarycentric* and *plotDotplot* functions from the triwise package (v.0.99.5) were used to generate the barycentric coordinates and the 2D hexagonal dotplot displaying the distribution of the detected genes. Genes of interest were manually specified and labeled. The modified code is accessible at the GitHub link outlined in the key resources table.

Pathway analysis was performed using the Single Cell Pathway Analysis (SCPA) tool on 3 Seurat objects (for pDCs, AS-DCs and cycling pDCs) comparing each of the tissues among the rest employing the *FindMarkers* function.

For human and mouse integration of pDC data, 3' scRNA-seq data of human BDCA2$^+$ cells from the four tissues extracted from this study was combined with 3' scRNA-seq of DCs sorted from six different tissues of C57BL/6 12 week-old male mice, as well data from a previous study containing pDCs[13]. The mouse DC data was bioinformatically subsetted to include only *Siglech*$^+$ cells. The resulting mouse and human *Seurat* objects were processed individually. Then, genes from the mouse dataset were converted into human orthologues. Only genes present in the human BDCA2$^+$ dataset and in the orthologue-converted mouse dataset were kept for further analysis, and the mouse and human *Seurat* objects were subsetted to include only those genes. Next, CCA-based integration was performed to obtain a single Seurat object containing both datasets. This dataset was used as the prediction dataset in a Random Forest Regression-based model made from the top 50 genes (Log_2 Fold Change > 0.75) of each cell type from the human dataset. This approach allowed an unbiased and integrated cross-species analysis. Specifically, for the Random Forest Regression model, the *randomForest* function was used with the transposed gene expression matrix from the human pDC dataset, using 50 samples per cell type category, and 1000 decision trees.

Diffusion map generation using CellRank: Diffusion map embeddings were computed from normalized single-cell RNA-seq data downloaded as h5ad files from the original publications of thymus[43], fetal tissues[46] or *.rds* file from the CD34 progenitor dataset[48]. Diffusion map embeddings and directed cell-cell transition matrices were constructed following the CellRank[47] pseudotime kernel vignette. Preprocessed single-cell RNA-seq data were first embedded using Palantir (v1.0+) to generate pseudotime estimates based on diffusion maps computed from AnnData objects in Scanpy (v1.9+). Palantir pseudotime values were subsequently utilized as the temporal covariate in CellRank (v1.5+), where the PseudotimeKernel method was applied to compute the transition matrix, capturing directed cellular dynamics without reliance on RNA velocity. Resulting fate probabilities and state transitions were visualized in low-dimensional UMAP space using CellRank's plotting functions, with all computation performed in reproducible Python scripts and analytical procedures mirroring CellRank's 300_pseudotime kernel tutorial (https://cellrank.readthedocs.io/en/latest/notebooks/tutorials/kernels/300_pseudotime.html).

Immunohistochemistry: FFPE tissue blocks used for this study were retrieved from the archive of the Department of Pathology (Spedali Civili di Brescia, Brescia, Italy). Human tissues included reactive neonatal thymus (n=3), adult BM (n=4), fetal thymus

from aborted pregnancies (n=4) and fetal lymph nodes from aborted pregnancies (n=3), and BM from biopsies of patients who have a diagnosis of BPDCN (n=5). Four-micron thick tissue sections were used for immunohistochemical staining. Sections were incubated with anti-BDCA2 antibody (clone 124B3,13, 1:100, Dendritics) or anti-IDH2 (polyclonal Rabbit, 1:200, Proteintech), the reaction was revealed using Novolink Polymer (Leica Microsystem) followed by DAB. For double staining, after completing the first immune reaction, the sections were incubated with anti-Ki67 (clone 30-9, Ready to use, Ventana) or anti E2.2/TCF4 (clone NCI-R159-6, 1:500, Abcam) and reactions were visualized using Mach 4 MR-AP (Biocare Medical), followed by VECTOR Blue.

Supplementary Material

Refer to Web version on PubMed Central for supplementary material.

Acknowledgements

We thank the patients and their families for providing permission to collect discarded tissues from surgical procedures. We thank Taylor Meritt (WUSM) for assistance in obtaining permission and sample collection; Amanda Swain (10x Genomics) for library preparation and helpful suggestions regarding the 10X protocol; Natalia Jaeger (Augusta University) for help with sample preparation; Simone Brioschi (WUSM) and Hao-Wei Chang (WUSM) for intellectual input; Dr. Erica Lantelme (WUSM) for the management of the flow cytometry core facility at the Pathology and Immunology Department (Washington University in St. Louis), and Pascaline Akitani (WUSM) and Dorjan Brinja (WUSM) for cell sorting. We thank the nurses of St Louis Children Hospital's pediatric OR for tonsil collection. We also thank the GTAC at the McDonnell Genome Institute at WUSM for scRNA-seq. GTAC is supported by the Washington University Institute of Clinical and Translational Sciences grant UL1TR002345 from NCATS of the NIH. W.V. is supported by AIRC IG Grant 2019-23179 and Fondazione Beretta (Brescia, Italy) for the Multiplex Platform.

References

1. Swiecki M, and Colonna M (2015). The multifaceted biology of plasmacytoid dendritic cells. Nat Rev Immunol 15. 10.1038/nri3865.
2. Reizis B. (2019). Plasmacytoid Dendritic Cells: Development, Regulation, and Function. Immunity 50, 37–50. 10.1016/j.immuni.2018.12.027. [PubMed: 30650380]
3. Asselin-Paturel C, and Trinchieri G (2005). Production of type I interferons. J Exp Med 202, 461–465. 10.1084/jem.20051395. [PubMed: 16103406]
4. Gilliet M, Cao W, and Liu Y-J (2008). Plasmacytoid dendritic cells: sensing nucleic acids in viral infection and autoimmune diseases. Nat Rev Immunol 8. 10.1038/nri2358.
5. Ewald SE, Lee BL, Lau L, Wickliffe KE, Shi G-P, Chapman HA, and Barton GM (2008). The ectodomain of Toll-like receptor 9 is cleaved to generate a functional receptor. Nature 456, 658–662. 10.1038/nature07405. [PubMed: 18820679]
6. Macal M, Lewis GM, Kunz S, Flavell R, Harker JA, and Zúñiga EI (2012). Plasmacytoid dendritic cells are productively infected and activated through TLR-7 early after arenavirus infection. Cell Host Microbe 11, 617–630. 10.1016/j.chom.2012.04.017. [PubMed: 22704622]
7. Rowland SL, Riggs JM, Gilfillan S, Bugatti M, Vermi W, Kolbeck R, Unanue ER, Sanjuan MA, and Colonna M (2014). Early, transient depletion of plasmacytoid dendritic cells ameliorates autoimmunity in a lupus model. Journal of Experimental Medicine 211. 10.1084/jem.20132620.
8. Sisirak V, Ganguly D, Lewis KL, Couillault C, Tanaka L, Bolland S, D'Agati V, Elkon KB, and Reizis B (2014). Genetic evidence for the role of plasmacytoid dendritic cells in systemic lupus erythematosus. Journal of Experimental Medicine 211. 10.1084/jem.20132522.
9. Soni C, Perez OA, Voss WN, Pucella JN, Serpas L, Mehl J, Ching KL, Goike J, Georgiou G, Ippolito GC, et al. (2020). Plasmacytoid Dendritic Cells and Type I Interferon Promote Extrafollicular B Cell Responses to Extracellular Self-DNA. Immunity 52, 1022–1038.e7. 10.1016/j.immuni.2020.04.015. [PubMed: 32454024]

10. Nehar-Belaid D, Hong S, Marches R, Chen G, Bolisetty M, Baisch J, Walters L, Punaro M, Rossi RJ, Chung C-H, et al. (2020). Mapping systemic lupus erythematosus heterogeneity at the single-cell level. Nat Immunol 21, 1094–1106. 10.1038/s41590-020-0743-0. [PubMed: 32747814]

11. Aung LL, Fitzgerald-Bocarsly P, Dhib-Jalbut S, and Balashov K (2010). Plasmacytoid dendritic cells in multiple sclerosis: Chemokine and chemokine receptor modulation by interferon-beta. J Neuroimmunol 226. 10.1016/j.jneuroim.2010.06.008.

12. Ah Kioon MD, Tripodo C, Fernandez D, Kirou KA, Spiera RF, Crow MK, Gordon JK, and Barrat FJ (2018). Plasmacytoid dendritic cells promote systemic sclerosis with a key role for TLR8. Sci Transl Med 10. 10.1126/scitranslmed.aam8458.

13. Rodrigues PF, Alberti-Servera L, Eremin A, Grajales-Reyes GE, Ivanek R, and Tussiwand R (2018). Distinct progenitor lineages contribute to the heterogeneity of plasmacytoid dendritic cells. Nat Immunol 19. 10.1038/s41590-018-0136-9.

14. Dress RJ, Dutertre C-A, Giladi A, Schlitzer A, Low I, Shadan NB, Tay A, Lum J, Kairi MFBM, Hwang YY, et al. (2019). Plasmacytoid dendritic cells develop from Ly6D+ lymphoid progenitors distinct from the myeloid lineage. Nat Immunol 20. 10.1038/s41590-019-0420-3.

15. Feng J, Pucella JN, Jang G, Alcántara-Hernández M, Upadhaya S, Adams NM, Khodadadi-Jamayran A, Lau CM, Stoeckius M, Hao S, et al. (2022). Clonal lineage tracing reveals shared origin of conventional and plasmacytoid dendritic cells. Immunity 55, 405–422.e11. 10.1016/j.immuni.2022.01.016. [PubMed: 35180378]

16. Rodrigues PF, Kouklas A, Cvijetic G, Bouladoux N, Mitrovic M, Desai JV, Lima-Junior DS, Lionakis MS, Belkaid Y, Ivanek R, et al. (2023). pDC-like cells are pre-DC2 and require KLF4 to control homeostatic CD4 T cells. Sci Immunol 8. 10.1126/sciimmunol.add4132.

17. Villani A-C, Satija R, Reynolds G, Sarkizova S, Shekhar K, Fletcher J, Griesbeck M, Butler A, Zheng S, Lazo S, et al. (2017). Single-cell RNA-seq reveals new types of human blood dendritic cells, monocytes, and progenitors. Science (1979) 356. 10.1126/science.aah4573.

18. See P, Dutertre C-A, Chen J, Günther P, McGovern N, Irac SE, Gunawan M, Beyer M, Händler K, Duan K, et al. (2017). Mapping the human DC lineage through the integration of high-dimensional techniques. Science (1979) 356. 10.1126/science.aag3009.

19. Leylek R, Alcántara-Hernández M, Lanzar Z, Lüdtke A, Perez OA, Reizis B, and Idoyaga J (2019). Integrated Cross-Species Analysis Identifies a Conserved Transitional Dendritic Cell Population. Cell Rep 29. 10.1016/j.celrep.2019.11.042.

20. Sulczewski FB, Maqueda-Alfaro RA, Alcántara-Hernández M, Perez OA, Saravanan S, Yun TJ, Seong D, Arroyo Hornero R, Raquer-McKay HM, Esteva E, et al. (2023). Transitional dendritic cells are distinct from conventional DC2 precursors and mediate proinflammatory antiviral responses. Nat Immunol 24, 1265–1280. 10.1038/s41590-023-01545-7. [PubMed: 37414907]

21. Mogilenko DA, Shpynov O, Andhey PS, Arthur L, Swain A, Esaulova E, Brioschi S, Shchukina I, Kerndl M, Bambouskova M, et al. (2021). Comprehensive Profiling of an Aging Immune System Reveals Clonal GZMK+ CD8+ T Cells as Conserved Hallmark of Inflammaging. Immunity 54, 99–115.e12. 10.1016/j.immuni.2020.11.005. [PubMed: 33271118]

22. Lepelletier Y, Zollinger R, Ghirelli C, Raynaud F, Hadj-Slimane R, Cappuccio A, Hermine O, Liu Y-J, and Soumelis V (2010). Toll-like receptor control of glucocorticoid-induced apoptosis in human plasmacytoid predendritic cells (pDCs). Blood 116, 3389–3397. 10.1182/blood-2010-05-282913. [PubMed: 20592251]

23. Hao Y, Hao S, Andersen-Nissen E, Mauck WM, Zheng S, Butler A, Lee MJ, Wilk AJ, Darby C, Zager M, et al. (2021). Integrated analysis of multimodal single-cell data. Cell 184, 3573–3587.e29. 10.1016/j.cell.2021.04.048. [PubMed: 34062119]

24. Korsunsky I, Millard N, Fan J, Slowikowski K, Zhang F, Wei K, Baglaenko Y, Brenner M, Loh P, and Raychaudhuri S (2019). Fast, sensitive and accurate integration of single-cell data with Harmony. Nat Methods 16. 10.1038/s41592-019-0619-0.

25. Hurwitz SN, Nkosi D, Conlon MM, York SB, Liu X, Tremblay DC, and Meckes DG (2017). CD63 Regulates Epstein-Barr Virus LMP1 Exosomal Packaging, Enhancement of Vesicle Production, and Noncanonical NF-κB Signaling. J Virol 91. 10.1128/JVI.02251-16.

26. Tognoli ML, Dancourt J, Bonsergent E, Palmulli R, de Jong OG, Van Niel G, Rubinstein E, Vader P, and Lavieu G (2023). Lack of involvement of CD63 and CD9 tetraspanins in the extracellular

vesicle content delivery process. Commun Biol 6, 532. 10.1038/s42003-023-04911-1. [PubMed: 37198427]

27. Lu N, Li Y, Zhang Z, Xing J, Sun Y, Yao S, and Chen L (2018). Human Semaphorin-4A drives Th2 responses by binding to receptor ILT-4. Nat Commun 9, 742. 10.1038/s41467-018-03128-9. [PubMed: 29467366]
28. Galpin KJC, Rodriguez GM, Maranda V, Cook DP, Macdonald E, Murshed H, Zhao S, McCloskey CW, Chruscinski A, Levy GA, et al. (2024). FGL2 promotes tumour growth and attenuates infiltration of activated immune cells in melanoma and ovarian cancer models. Sci Rep 14, 787. 10.1038/s41598-024-51217-1. [PubMed: 38191799]
29. Shaebani MR, Stankevicins L, Vesperini D, Urbanska M, Flormann DAD, Terriac E, Gad AKB, Cheng F, Eriksson JE, and Lautenschläger F (2022). Effects of vimentin on the migration, search efficiency, and mechanical resilience of dendritic cells. Biophys J 121, 3950–3961. 10.1016/j.bpj.2022.08.033. [PubMed: 36056556]
30. Winkler TH, and Mårtensson I-L (2018). The Role of the Pre-B Cell Receptor in B Cell Development, Repertoire Selection, and Tolerance. Front Immunol 9. 10.3389/fimmu.2018.02423.
31. Cisse B, Caton ML, Lehner M, Maeda T, Scheu S, Locksley R, Holmberg D, Zweier C, den Hollander NS, Kant SG, et al. (2008). Transcription Factor E2-2 Is an Essential and Specific Regulator of Plasmacytoid Dendritic Cell Development. Cell 135, 37–48. 10.1016/j.cell.2008.09.016. [PubMed: 18854153]
32. Asselin-Paturel C, Brizard G, Chemin K, Boonstra A, O'Garra A, Vicari A, and Trinchieri G (2005). Type I interferon dependence of plasmacytoid dendritic cell activation and migration. J Exp Med 201, 1157–1167. 10.1084/jem.20041930. [PubMed: 15795237]
33. Wu K, Yang Y, Wang C, Davoli MA, D'Amico M, Li A, Cveklova K, Kozmik Z, Lisanti MP, Russell RG, et al. (2003). DACH1 inhibits transforming growth factor-beta signaling through binding Smad4. J Biol Chem 278, 51673–51684. 10.1074/jbc.M310021200. [PubMed: 14525983]
34. Coenen I, de Jong E, Jones AC, Khoo S-K, Foo S, Howland SW, Ginhoux F, Le Souëf PN, Holt PG, Strickland DH, et al. (2024). Impaired interferon response in plasmacytoid dendritic cells from children with persistent wheeze. J Allergy Clin Immunol 153, 1083–1094. 10.1016/j.jaci.2023.11.920. [PubMed: 38110059]
35. Zhao Y, Su H, Shen X, Du J, Zhang X, and Zhao Y (2017). The immunological function of CD52 and its targeting in organ transplantation. Inflammation Research 66, 571–578. 10.1007/s00011-017-1032-8. [PubMed: 28283679]
36. Arroyo Hornero R, Maqueda-Alfaro RA, Solís-Barbosa MA, Leylek RA, Medina Chavez O, Martinez OM, Gottfried-Blackmore A, and Idoyaga J (2025). TNF and type I interferon crosstalk controls the fate and function of plasmacytoid dendritic cells. Nat Immunol 26, 1540–1552. 10.1038/s41590-025-02234-3. [PubMed: 40796660]
37. Cham LB, Gunst JD, Schleimann MH, Frattari GS, Rosas-Umbert M, Vibholm LK, van der Sluis RM, Jakobsen MR, Olesen R, Lin L, et al. (2023). Single cell analysis reveals a subset of cytotoxic-like plasmacytoid dendritic cells in people with HIV-1. iScience 26, 107628. 10.1016/j.isci.2023.107628. [PubMed: 37664600]
38. Wu Y, Yang S, Ma J, Chen Z, Song G, Rao D, Cheng Y, Huang S, Liu Y, Jiang S, et al. (2022). Spatiotemporal Immune Landscape of Colorectal Cancer Liver Metastasis at Single-Cell Level. Cancer Discov 12, 134–153. 10.1158/2159-8290.CD-21-0316. [PubMed: 34417225]
39. Zhan Y, Chow KV, Soo P, Xu Z, Brady JL, Lawlor KE, Masters SL, O'keeffe M, Shortman K, Zhang J-G, et al. (2016). Plasmacytoid dendritic cells are short-lived: reappraising the influence of migration, genetic factors and activation on estimation of lifespan. Sci Rep 6, 25060. 10.1038/srep25060. [PubMed: 27112985]
40. Kawamoto H, Ohmura K, Fujimoto S, Lu M, Ikawa T, and Katsura Y (2003). Extensive proliferation of T cell lineage-restricted progenitors in the thymus: an essential process for clonal expression of diverse T cell receptor β chains. Eur J Immunol 33, 606–615. 10.1002/eji.200323461. [PubMed: 12616481]
41. von Boehmer H, and Fehling HJ (1997). STRUCTURE AND FUNCTION OF THE PRE-T CELL RECEPTOR. Annu Rev Immunol 15, 433–452. 10.1146/annurev.immunol.15.1.433. [PubMed: 9143695]

42. Domínguez Conde C, Xu C, Jarvis LB, Rainbow DB, Wells SB, Gomes T, Howlett SK, Suchanek O, Polanski K, King HW, et al. (2022). Crosstissue immune cell analysis reveals tissue-specific features in humans. Science (1979) 376. 10.1126/science.abl5197.
43. Park J-E, Botting RA, Domínguez Conde C, Popescu D-M, Lavaert M, Kunz DJ, Goh I, Stephenson E, Ragazzini R, Tuck E, et al. (2020). A cell atlas of human thymic development defines T cell repertoire formation. Science (1979) 367. 10.1126/science.aay3224.
44. Zeng AGX, Iacobucci I, Shah S, Mitchell A, Wong G, Bansal S, Chen D, Gao Q, Kim H, Kennedy JA, et al. (2025). Single-cell Transcriptional Atlas of Human Hematopoiesis Reveals Genetic and Hierarchy-Based Determinants of Aberrant AML Differentiation. Blood Cancer Discov 6, 307–324. 10.1158/2643-3230.BCD-24-0342. [PubMed: 40294241]
45. Madissoon E, Wilbrey-Clark A, Miragaia RJ, Saeb-Parsy K, Mahbubani KT, Georgakopoulos N, Harding P, Polanski K, Huang N, Nowicki-Osuch K, et al. (2020). scRNA-seq assessment of the human lung, spleen, and esophagus tissue stability after cold preservation. Genome Biol 21, 1. 10.1186/s13059-019-1906-x.
46. Suo C, Dann E, Goh I, Jardine L, Kleshchevnikov V, Park J-E, Botting RA, Stephenson E, Engelbert J, Tuong ZK, et al. (2022). Mapping the developing human immune system across organs. Science (1979) 376. 10.1126/science.abo0510.
47. Weiler P, Lange M, Klein M, Pe'er D, and Theis F (2024). CellRank 2: unified fate mapping in multiview single-cell data. Nat Methods 21, 1196–1205. 10.1038/s41592-024-02303-9. [PubMed: 38871986]
48. Ulezko Antonova A, Lonardi S, Monti M, Missale F, Fan C, Coates ML, Bugatti M, Jaeger N, Fernandes Rodrigues P, Brioschi S, et al. (2023). A distinct human cell type expressing MHCII and RORγt with dual characteristics of dendritic cells and type 3 innate lymphoid cells. Proc Natl Acad Sci U S A 120, e2318710120. 10.1073/pnas.2318710120. [PubMed: 38109523]
49. Esashi E, Wang Y-H, Perng O, Qin X-F, Liu Y-J, and Watowich SS (2008). The signal transducer STAT5 inhibits plasmacytoid dendritic cell development by suppressing transcription factor IRF8. Immunity 28, 509–520. 10.1016/j.immuni.2008.02.013. [PubMed: 18342552]
50. Abdalla AEA, Abdulgayoom M, Al-Mashdali AF, Ibrahim F, Gangat N, and Mohamed SF (2025). Plasmacytoid Dendritic Cell-Expansion in Acute Myeloid Leukemia (pDC-AML): a Review of Clinicopathologic Features, Genetics, and Outcomes. Curr Hematol Malig Rep 20, 19. 10.1007/s11899-025-00761-2. [PubMed: 41191126]
51. Mehrotra P, Maschalidi S, Boeckaerts L, Maueröder C, Tixeira R, Pinney J, Burgoa Cardás J, Sukhov V, Incik Y, Anderson Christopher.J., et al. (2024). . Oxylipins and metabolites from pyroptotic cells act as promoters of tissue repair. Nature 631, 207–215. 10.1038/s41586-024-07585-9. [PubMed: 38926576]
52. Lavaert M, Liang KL, Vandamme N, Park J-E, Roels J, Kowalczyk MS, Li B, Ashenberg O, Tabaka M, Dionne D, et al. (2020). Integrated scRNA-Seq Identifies Human Postnatal Thymus Seeding Progenitors and Regulatory Dynamics of Differentiating Immature Thymocytes. Immunity 52, 1088–1104.e6. 10.1016/j.immuni.2020.03.019. [PubMed: 32304633]
53. Liang KL, Roels J, Lavaert M, Putteman T, Boehme L, Tilleman L, Velghe I, Pegoretti V, Van de Walle I, Sontag S, et al. (2023). Intrathymic dendritic cell-biased precursors promote human T cell lineage specification through IRF8-driven transmembrane TNF. Nat Immunol 24, 474–486. 10.1038/s41590-022-01417-6. [PubMed: 36703005]
54. Anselmi G, Vaivode K, Dutertre C-A, Bourdely P, Missolo-Koussou Y, Newell E, Hickman O, Wood K, Saxena A, Helft J, et al. (2020). Engineered niches support the development of human dendritic cells in humanized mice. Nat Commun 11, 2054. 10.1038/s41467-020-15937-y. [PubMed: 32345968]
55. Cuglievan B, Connors J, He J, Khazal S, Yedururi S, Dai J, Garces S, Quesada AE, Roth M, Garcia M, et al. (2023). Blastic plasmacytoid dendritic cell neoplasm: a comprehensive review in pediatrics, adolescents, and young adults (AYA) and an update of novel therapies. Leukemia 37, 1767–1778. 10.1038/s41375-023-01968-z. [PubMed: 37452102]
56. Griffin GK, Booth CAG, Togami K, Chung SS, Ssozi D, Verga JA, Bouyssou JM, Lee YS, Shanmugam V, Hornick JL, et al. (2023). Ultraviolet radiation shapes dendritic cell leukaemia transformation in the skin. Nature 618, 834–841. 10.1038/s41586-023-06156-8. [PubMed: 37286599]

57. Taylor J, Haddadin M, Upadhyay VA, Grussie E, Mehta-Shah N, Brunner AM, Louissaint A, Lovitch SB, Dogan A, Fathi AT, et al. (2019). Multicenter analysis of outcomes in blastic plasmacytoid dendritic cell neoplasm offers a pretargeted therapy benchmark. Blood 134, 678–687. 10.1182/blood.2019001144. [PubMed: 31243042]
58. Lande R, Ganguly D, Facchinetti V, Frasca L, Conrad C, Gregorio J, Meller S, Chamilos G, Sebasigari R, Riccieri V, et al. (2011). Neutrophils activate plasmacytoid dendritic cells by releasing self-DNA-peptide complexes in systemic lupus erythematosus. Sci Transl Med 3, 73ra19. 10.1126/scitranslmed.3001180.
59. Pucella JN, Maqueda-Alfaro RA, Ni H, Bandeira Sulczewski F, Eichinger A, Esteva E, Ra AC, Das A, Perez OA, Feng J, et al. (2025). Tonic type I interferon signaling optimizes the antiviral function of plasmacytoid dendritic cells. Nat Immunol 26, 1946–1961. 10.1038/s41590-025-02279-4. [PubMed: 41087726]
60. Arpaia N, and Barton GM (2011). Toll-like receptors: key players in antiviral immunity. Curr Opin Virol 1, 447–454. 10.1016/j.coviro.2011.10.006. [PubMed: 22440908]
61. Sasai M, Linehan MM, and Iwasaki A (2010). Bifurcation of Toll-like receptor 9 signaling by adaptor protein 3. Science 329, 1530–1534. 10.1126/science.1187029. [PubMed: 20847273]
62. Cella M, Jarrossay D, Facchetti F, Alebardi O, Nakajima H, Lanzavecchia A, and Colonna M (1999). Plasmacytoid monocytes migrate to inflamed lymph nodes and produce large amounts of type I interferon. Nat Med 5. 10.1038/11360.
63. Ashby KM, Vobořil M, Salgado OC, Lee ST, Martinez RJ, O'Connor CH, Breed ER, Xuan S, Roll CR, Bachigari S, et al. (2024). Sterile production of interferons in the thymus affects T cell repertoire selection. Sci Immunol 9. 10.1126/sciimmunol.adp1139.
64. Xue L, Salimi M, Panse I, Mjösberg JM, McKenzie ANJ, Spits H, Klenerman P, and Ogg G (2014). Prostaglandin D2 activates group 2 innate lymphoid cells through chemoattractant receptor-homologous molecule expressed on TH2 cells. Journal of Allergy and Clinical Immunology 133, 1184–1194.e7. 10.1016/j.jaci.2013.10.056. [PubMed: 24388011]
65. Henault J, Riggs JM, Karnell JL, Liarski VM, Li J, Shirinian L, Xu L, Casey KA, Smith MA, Khatry DB, et al. (2016). Self-reactive IgE exacerbates interferon responses associated with autoimmunity. Nat Immunol 17, 196–203. 10.1038/ni.3326. [PubMed: 26692173]
66. Smith N, Pietrancosta N, Davidson S, Dutrieux J, Chauveau L, Cutolo P, Dy M, Scott-Algara D, Manoury B, Zirafi O, et al. (2017). Natural amines inhibit activation of human plasmacytoid dendritic cells through CXCR4 engagement. Nat Commun 8. 10.1038/ncomms14253.
67. Cella M, Jarrossay D, Facchetti F, Alebardi O, Nakajima H, Lanzavecchia A, and Colonna M (1999). Plasmacytoid monocytes migrate to inflamed lymph nodes and produce large amounts of type I interferon. Nat Med 5, 919–923. 10.1038/11360. [PubMed: 10426316]
68. Ghirelli C, Zollinger R, and Soumelis V (2010). Systematic cytokine receptor profiling reveals GM-CSF as a novel TLR-independent activator of human plasmacytoid predendritic cells. Blood 115, 5037–5040. 10.1182/blood-2010-01-266932. [PubMed: 20382843]
69. Yoshida H, Lareau CA, Ramirez RN, Rose SA, Maier B, Wroblewska A, Desland F, Chudnovskiy A, Mortha A, Dominguez C, et al. (2019). The cis- Regulatory Atlas of the Mouse Immune System. Cell 176, 897–912.e20. 10.1016/j.cell.2018.12.036. [PubMed: 30686579]

Highlights

- pDCs adopt tissue-enriched IFN-I, NF-κB, and resting states
- A pDC state present in all tissues makes PGD2 and responds to dopamine
- Cycling pDCs arise in fetal and infant lymphoid sites and persist in bone marrow lifelong
- Cycling pDCs carrying mutations are enriched in bone marrow in pDC neoplasm

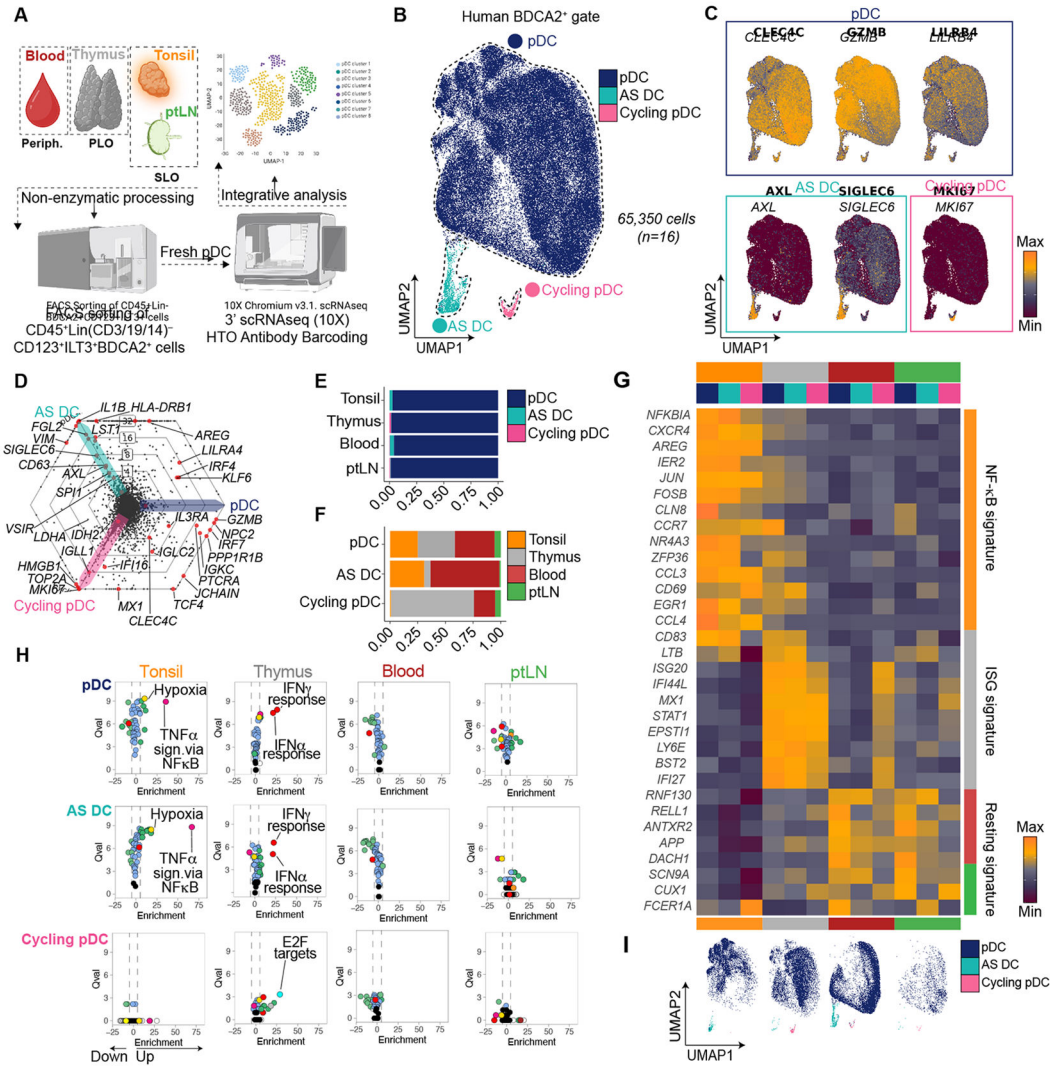

Figure 1. Lin^{-}BDCA2^{+} cells contain pDCs, AS-DCs, and cycling pDCs.

(**A**) Diagram of workflow.

(**B**) UMAP of all sequenced BDCA2^{+} cells identifies pDCs (dark blue), AS-DCs (light blue) and cycling pDCs (pink). Periph, periphery; PLO, primary lymphoid organs; SLO, secondary lymphoid organs.

(**C**) Gene expression plots of marker genes for each cluster.

(**D**) Radar plot showing discriminating genes for pDCs, AS-DCs and cycling pDCs; red dots represent labeled genes. Genes along the line from the plot's center to a cell type vertex are unique to that cell type; those between two vertices represent genes shared by both cell types.

(**E** and **F**) Bar plot showing the normalized distribution of each cell type across each tissue (**E**) and each tissue across cell type (**F**).

(**G**) Heatmap of marker genes (Log_2 Fold Change>0.75) and their average expression in each cell type by tissue.

(**H**) Pathway enrichment analysis (SCPA) for each cell type in each tissue. X axes represent upregulated (right) or downregulated (left) pathways; Y axes represent Q values.

(**I**) UMAP plots split by tissue of origin and colored by cell type (from B).

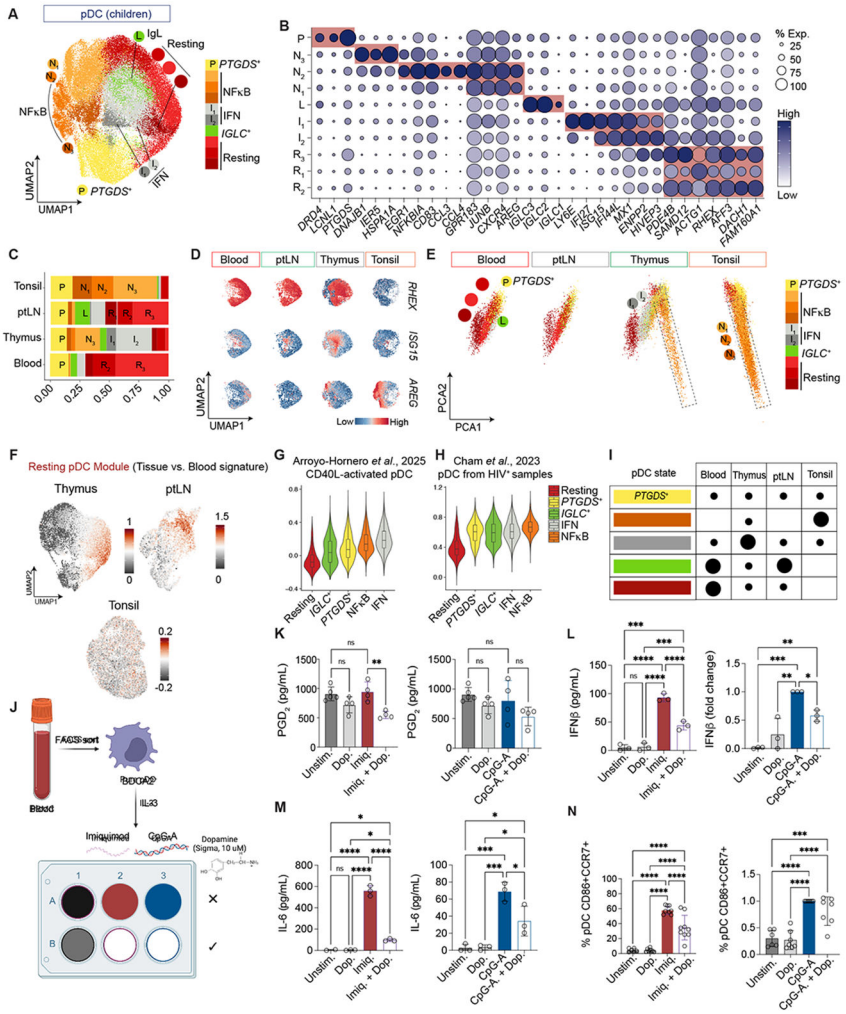

Figure 2. pDCs show different states within tissues.

(**A**) UMAP of pDCs from children's blood, ptLN, thymus, and tonsil; colors match organ coding in Fig. 1F.

(**B**) Dot plot of top DEGs in each cluster in (A).

(**C**) Bar plot of normalized abundance of each cluster in each tissue.

(**D**) UMAPs showing gene expression plots for *RHEX*, *ISG15* and *AREG* in different tissues.

(**E**) PCA projection of clusters from A, showing PC1 and PC2, split by tissue of origin. The rectangle highlights clusters N_1-N_3.

(**F**) Projection of the resting pDC module onto pDCs from different tissues.

(**G** and **H**) Violin plot of module enrichment from CD40L activated pDCs[36] (**G**) and HIV-laiden pDCs[37] (**H**) onto clusters from (A).

(**I**) Table summarizing cluster distribution across tissues; large circles indicate higher abundance.

(**J-N**) Experimental workflow (**J**), and quantification of PGD_2 (**K**), IFN-β (**L**) and IL-6 production (**M**), and frequency of $CD86^+CCR7^+$ cells (**N**) in purified pDCs stimulated with Imiquimod or CpG-A, in presence or absence of dopamine. From at least three independent

biological replicates, each data point represents a biological replicate (mean), and errors bars show SD.*p < 0.05, **p < 0.01, ***p < 0.001, ****p < 0.0001 on two-way ANOVA.

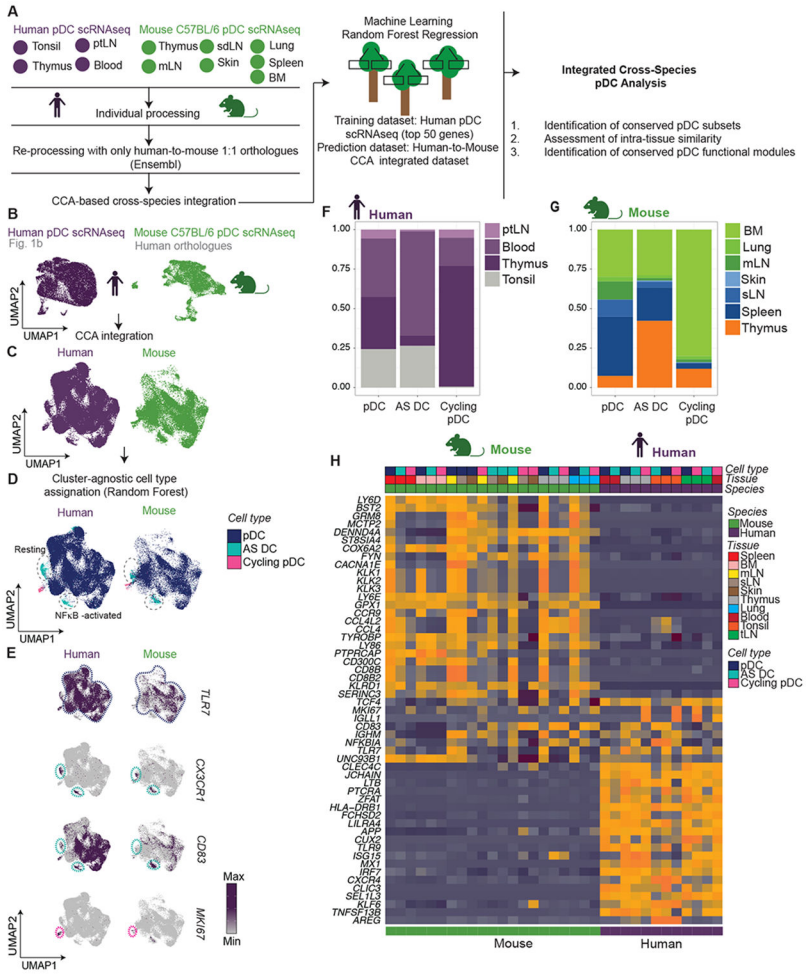

Figure 3. Integration of human and mouse pDC signatures.

(**A**) Analytical workflow of across species data integration from human and mouse pDCs tissues.

(**B-E**) UMAP plots of individually processed human and mouse datasets using human orthologues of the mouse genes (**B**), CCA-integrated datasets split by species (**C**) and split by cell type assignment (**D**), and signature marker genes for pDCs, AS-DCs and cycling pDCs conserved between human and mouse (**E**).

(**F** and **G**) Organ distribution of pDCs, AS-DCs and cycling pDCs in human (**F**) and mouse (**G**) tissues.

(**H**) Heat map showing the mean expression of genes that discriminate mouse pDCs (top) from human pDCs (bottom); shared genes are shown in the middle.

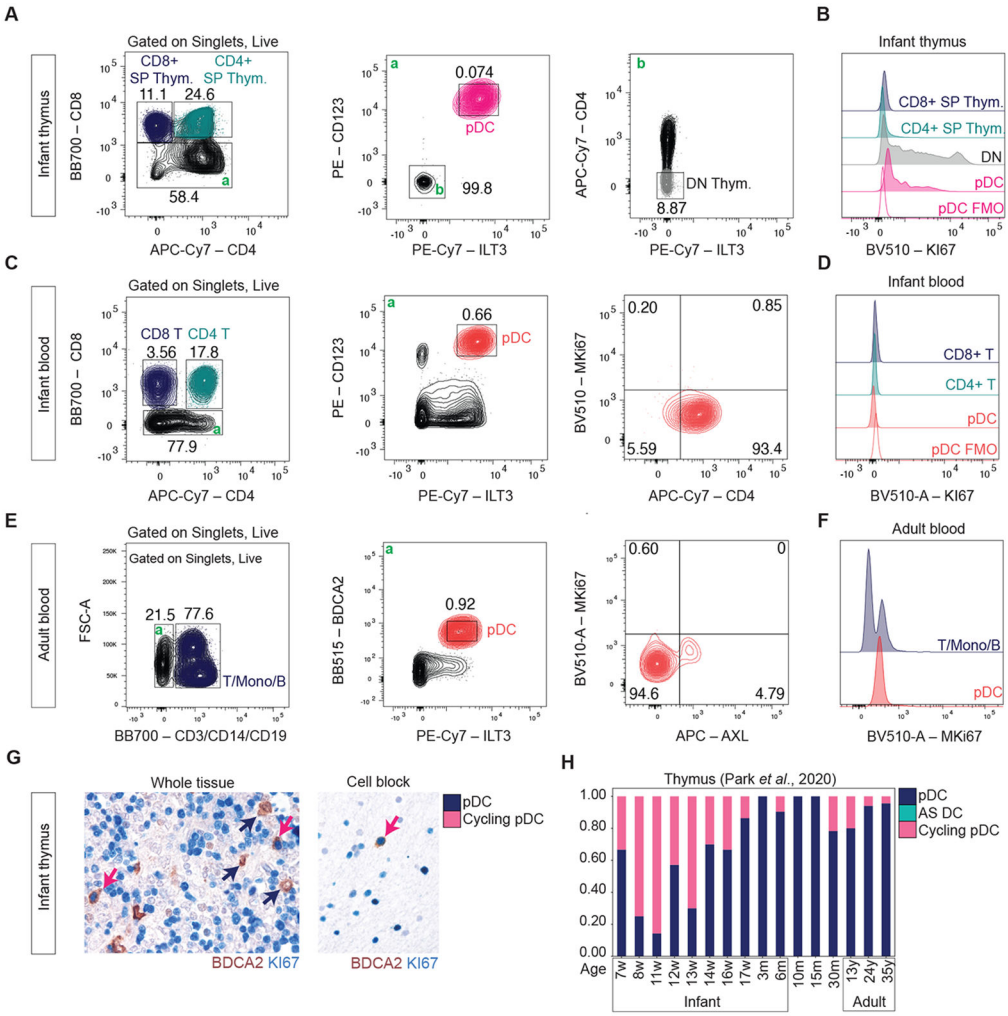

Figure 4. Infant thymus contains cycling pDCs.

(**A-F**) Flow cytometric identification of pDCs and other immune cells (**A,C,E**) and staining of Ki-67 (**B,D,F**) in infant thymus (**A,B**), infant blood from the same donor (**C,D**) and adult blood (**E,F**). One representative donor of three is shown. FMO, Fluorescence Minus One. (**G**) Immunohistochemistry of whole thymic tissue (left) and cytology cell block of thymocytes (right) stained for BDCA2 (brown) and Ki-67 (blue). Red arrows: BDCA2^{+}Ki-67^{+}; dark blue arrows: BDCA2^{+}Ki-67^{-} cells. H Bar graph of abundance of pDCs, AS-DCs and cycling pDC from a thymus atlas[43].

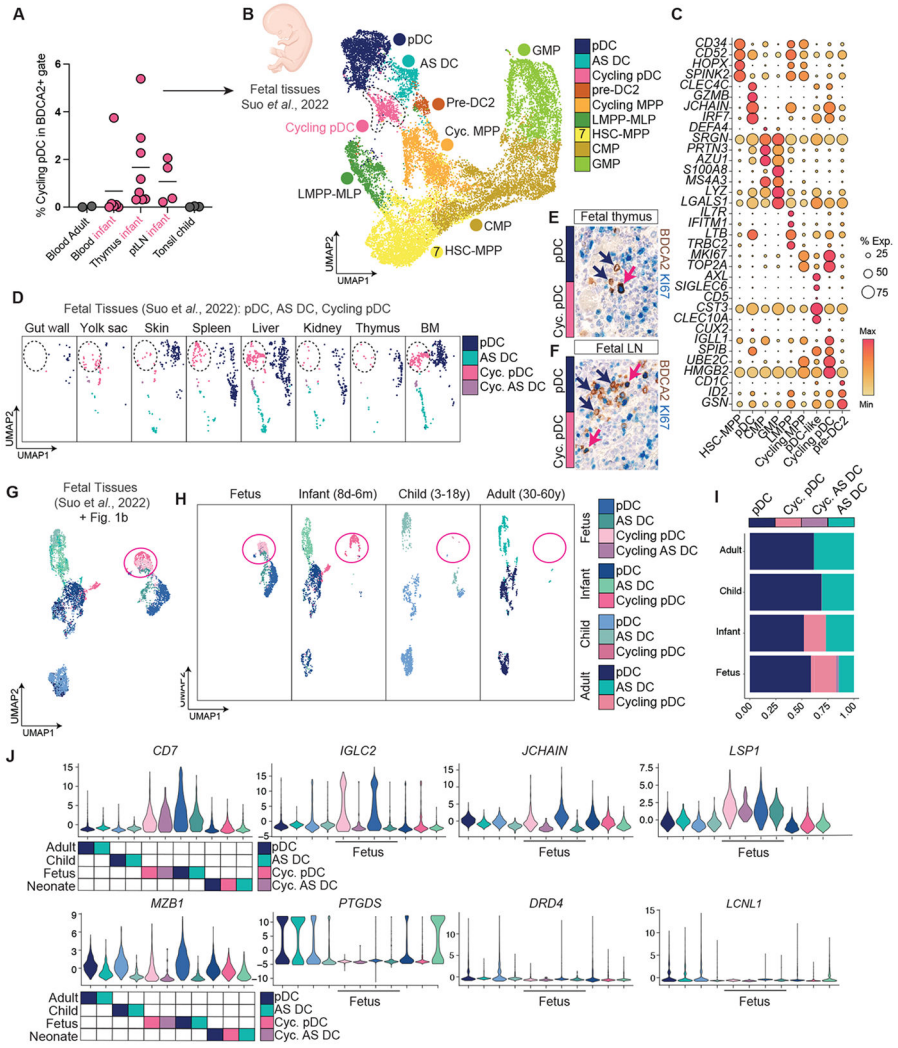

Figure 5. Cycling pDCs are enriched in fetal lymphoid organs.

(**A**)Percentages of cycling pDCs in the scRNA-seq samples from our study; infant tissues are highlighted in pink.

(**B**) UMAP showing a selected group of cells from the Fetal Tissue Atlas[46] manually reprocessed and re-annotated.

(**C**) Dot plot of discriminating genes for clusters in (B).

(**D**) UMAPs for pDCs, AS-DCs and cycling pDCs from (B) split by tissue of origin, with cycling AS-DCs annotated as a distinct group.

(**E** and **F**) Immunohistochemistry of fetal thymus (**E**) and fetal lymph nodes (**F**) stained for BDCA2 (brown) and Ki-67 (blue); pink arrows mark double-positive cells, while dark blue arrows mark BDCA2^{+}Ki-67^{-} cells.

(**G** and **H**) UMAP plots showing cells from (**G**) a dataset merging cells in (D) with cells in Fig. 1B, after random down-sampling to equalize cell numbers colored by cell type and (**H**) cells from this merged dataset split by age group.

(**I**) Abundances of cell types in H.

(**J**) Violin plots showing expression of selected genes from pDCs, AS-DCs cycling pDCs from fetuses, infants, children and adults. Fetus-derived clusters are highlighted in grey.

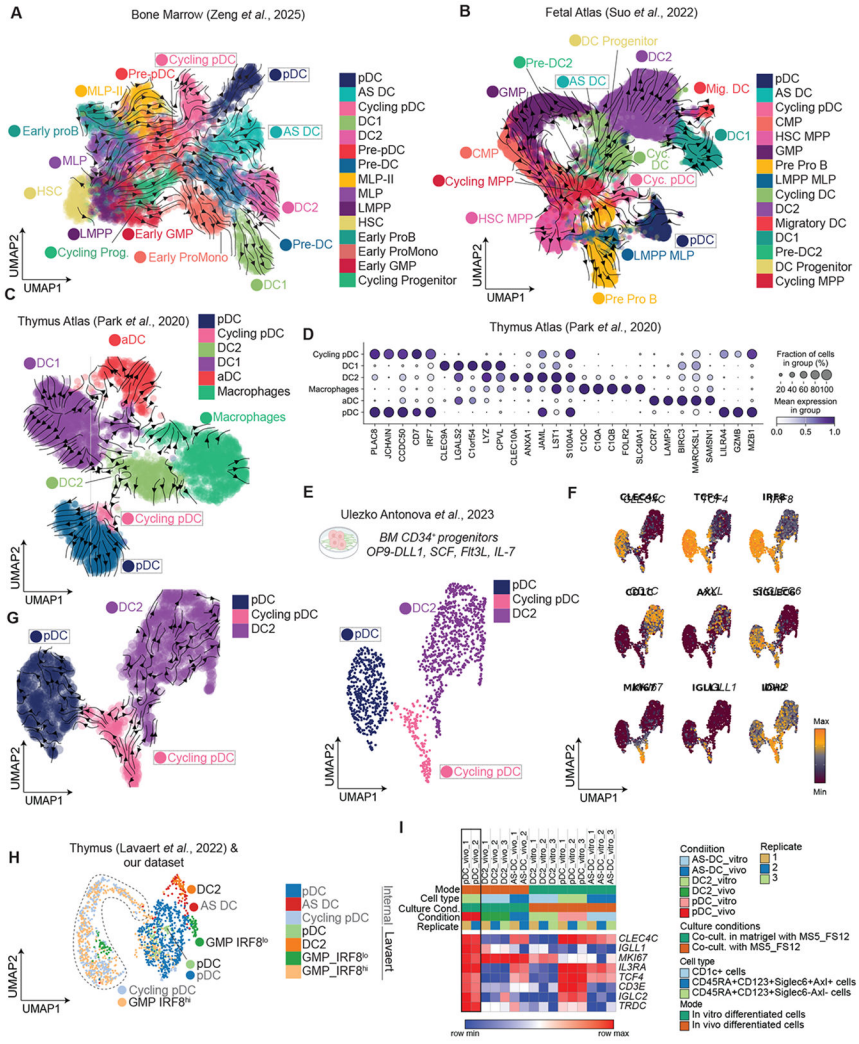

Figure 6. Cycling pDCs preceed pDCs and pre-DCs/DC2s.

(**A-D**) Diffusion maps showing pseudotime and k-nearest neighbor-based developmental trajectories for selected clusters from a BM Atlas[44] (**A**), a Fetal Tissue Atlas[46] (**B**) and a thymus atlas[43] (**C**); cluster names match the original publication except for (C), where cell cluster name was re-assigned based on the top five expressed genes as shown in the dot plot in (**D**).

(**E** and **F**) UMAP plots showing reclustering of proliferating cells, pDCs and DC2s from CD34 cultures[48] (**E**) and expression of selected genes that identify pDCs, cycling pDCs and DC2s (**F**).

(**G**) Diffusion map showing developmental trajectories for cells in (E).

(**H**) UMAP plot showing integration of 1,000 cells from Fig. 1B and 1,000 pDCs, DC2s and Granulocyte-Monocyte Precursors (GMP) derived from a dataset of thymic precursors[52].

(**I**) Heatmap showing canonical cycling pDC genes in a bulk RNA-seq dataset of DC subsets derived from cord blood hematopoietic cells[54].

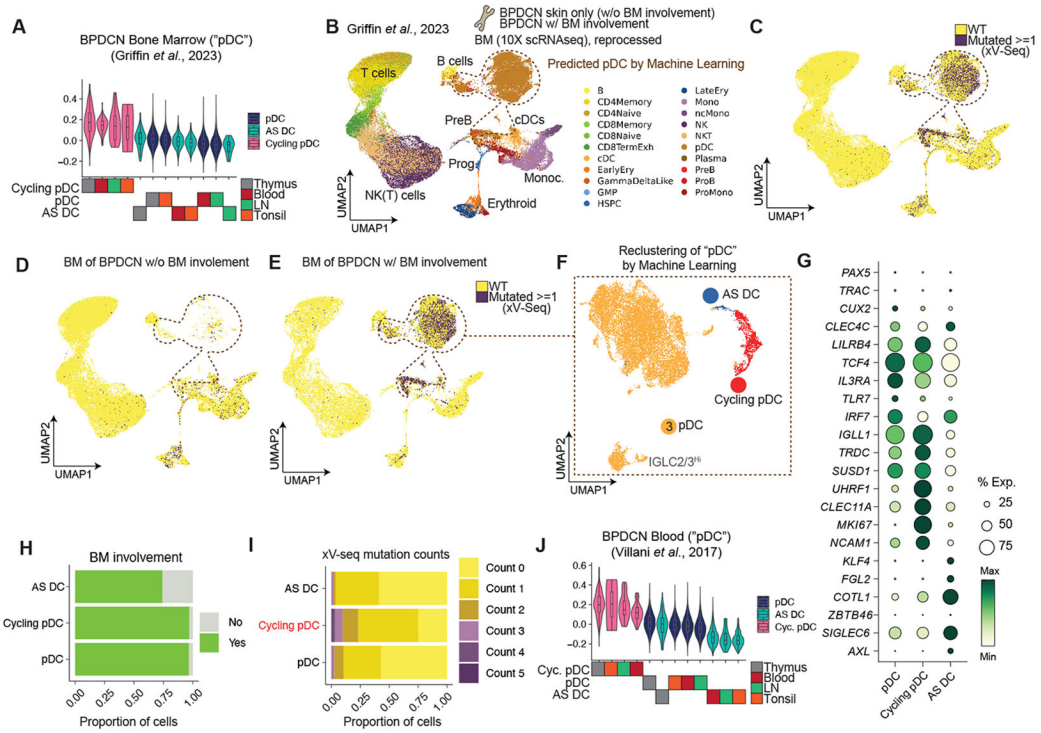

Figure 7. Cycling pDCs are expanded and hypermutated in BM of BPDCN patients.

(**A**) Violin plot displaying ranked module score enrichment of the BM BPDCN signature[69] onto our dataset from Fig. 1B. The signature was obtained by comparing pDCs from BPDCN patients with BM involvement to those in patients without BM involvement. Organ of origin is indicated.

(**B** and **C**) UMAP plot showing reanalysis of BPDCN patient samples with and without BM involvement[53] (**B**) and cells bearing no mutations (yellow) or one or more mutations (purple) (**C**). In C cluster labels follow the authors' Random Forest approach; the discontinuous line marks cells predicted as pDCs (light brown).

(**D** and **E**) UMAP of cells in B split by patients without BM involvement (**D**) or with BM involvement (**E**). Cells classified as pDCs are outlined with a dotted line.

(**F**) UMAP plot of cells re-analyzed from[53] and classified as AS-DCs, pDCs and cycling pDCs based on our scRNA-seq analysis (Fig.1B).

(**G**) Dot plot of discriminative genes for clusters in F.

(**H** and **I**) Bar graph quantifying abundance of each subset in patients without or with BM involvement (**I**), and mutation occurrences in each subset (**H**).

(**J**) Violin plot of ranked module score enrichment of blood BPDCN signature[17] obtained by comparing blood pDCs in BPDCN patients vs. controls projected onto our dataset.

Key Resource Table

REAGENT or RESOURCE	SOURCE	IDENTIFIER
Antibodies		
CD303 FITC Clone AC144	Miltenyi	Cat# 130-113-192
CD14 PerCP/Cy5.5 Clone QA18A22	Biolegend	Cat# 398711
CD3 PerCP/Cy5.5 Clone OKT3	Biolegend	Cat# 317336
CD19 PerCP/Cy5.5 Clone HIB19	Biolegend	Cat# 982412
CD1c BV605 Clone L161	Biolegend	Cat# 331537
CD11c BV510 Clone S-HCL-3	Biolegend	Cat# 371513
AXL APC Clone S21005B	Biolegend	Cat# 386205
CD85g BV421 Clone 17G10.2	Biolegend	Cat# 326419
Ki-67 BV421 Clone Ki-67	Biolegend	Cat# 350505
CD34 BV605 Clone 581	Biolegend	Cat# 343629
CD34 PE/Dazzle594 clone 581	Biolegend	Cat# 343533
CD45 BUV395 Clone HI30	BD Horizon	Cat# 563792
CD4 BUV661 Clone SK3	BD Horizon	Cat# 51-9013239
CD135 Biotin Clone A2F10.1	Biolegend	Cat# 135308
CD1c BV510 Clone L161	Biolegend	Cat# 331533
Ki-67 BV510 Clone Ki-67	Biolegend	Cat# 350517
CD86 PE Clone BU63	Biolegend	Cat# 374205
CD123 PE Clone S18016C	Biolegend	Cat# 396603
TotalSeq Hashtag 1 Antibody	Biolegend	Cat# 394631
TotalSeq Hashtag 2 Antibody	Biolegend	Cat# 394633
TotalSeq Hashtag 3 Antibody	Biolegend	Cat# 394635
TotalSeq hHashtag 1 Antibody	Biolegend	Cat# 394631
TotalSeq hHashtag 2 Antibody	Biolegend	Cat# 394633
TotalSeq hHashtag 3 Antibody	Biolegend	Cat# 394635
TotalSeq mHashtag 1 Antibody	Biolegend	Cat# 155831
TotaSeq mHashtag 2 Antibody	Biolegend	Cat# 155833
TotalSeq mHashtag 3 Antibody	Biolegend	Cat# 155835
TotalSeq mHashtag 5 Antibody	Biolegend	Cat# 155837
TotalSeq mHashtag 5 Antibody	Biolegend	Cat# 155839
TotalSeq mHashtag 6 Antibody	Biolegend	Cat# 155841
TotalSeq mHashtag 7 Antibody	Biolegend	Cat# 155843
TotalSeq mHashtag 8 Antibody	Biolegend	Cat# 155845
TotalSeq mHashtah 9 Antibody	Biolegend	Cat# 155847
CD303 Clone 124B3.13	Dendritics (Novus Biologicals)	Cat# DDX0043P-100
Ki-67 Clone 30.9	Ventana/Roche	Cat# 05278384001
Biological Samples		

REAGENT or RESOURCE	SOURCE	IDENTIFIER
Thymus	IRB 202009010	St Louis Children Hospital
Perithymic lymph nodes	IRB 202009010	St Louis Children Hospital
Blood (children)	IRB 202009010	St Louis Children Hospital
Tonsils	IRB	St Louis Children Hospital
Blood (adults)	IRB	American Red Cross
Software and Algorithms		
Cell Ranger v2.0.0 and v6.0.0	10x Genomics	N/A
GraphPad Prism	Dotmatics	https://www.graphpad.com/features
FlowJo (v10)	TreeStar	https://www.flowjo.com/solutions/flowjo/
Illustrator	Adobe	https://www.adobe.com/products/catalog.html
R 4.4	The R Foundation	https://www.r-project.org
Seurat v4	Hao *et al.*, 2023	https://satijalab.org/seurat/
Cellrank v2.07	Weiler *et al.*, 2024	https://cellrank.readthedocs.io/en/latest/notebooks/tutorials/kernels/300_pseudotime.html
Python v3.10.18	Python Software Foundation	https://www.python.org/
Reagents and Kits		
PGD2 ELISA kit	MyBiosource	Cat# MBS2515877
BDCA4 Microbead kit	Miltenyi	Cat# 13-090-53
FOXP3/TF Staining Buffer set	eBioscience	Cat# 00-5523-00
Human Interferon-β ELISA kit	PBL	Cat# 41410
Human Inflammatory Cytokine CBA	BD	Cat# 551811
Chemicals, peptides, recombinant proteins and others		
7AAD Viability Staining	Biolegend	Cat# 420404
1M HEPES Buffer	Corning	Cat# 25-060-Cl
Beta-Mercaptoethanol	Sigma	Cat# M-7522
Dopamine hydrochloride	Sigma	Cat# H8502
Bovine Serum Albumin (BSA)	Rockland	Cat# BSA-1000
EDTA	Corning	Cat# 46-034-Cl
Glutamax (100x)	Gibco	Cat# 35050-061
Human Flt3L	Supernatant	Produced in house
Kanamycin Sulfate (100x)	Gibco	Cat# 15160-054
MEM Nonessential amino acids (100x)	Corning	Cat# 25-025-Cl
PBS (1x)	Leinco	Cat# P364
RPMI 1640	Sigma	Cat# R8758-1L
SAV BV661	BD horizon	Cat# 612979
Sodium Pyruvate 100mM	Corning	Cat# 25-000-Cl
Hyclone Iron-Supplemented Calf Serum	Cytiva	Cat# SH30072.04
Human GM-CSF	Peprotech	Cat# 300-03-20UG
Human SCF	Peprotech	Cat# 300-07-10UG

REAGENT or RESOURCE	SOURCE	IDENTIFIER
Human IL-3	Peprotech	Cat# 200-03-10UG
Percoll	Cytiva	Cat# 45-001-747
Imiquimod	InVivogen	Cat# tlrl-imqs-1
CpG-A ODN 2216	InVivogen	Cat# tlrl-2216
Ficoll-Paque PLUS Media	Cytiva	Cat# 45-001-750
Deposited Data and Code		https://github.com/aulezko/
Human pDC scRNAseq Data	This paper	GEO: GSE273852
Mouse pDC scRNAseq Data	This paper	GEO: GSE314567
BM Atlas	Zeng *et al.*, 2025	https://cellxgene.cziscience.com/e/cd2f23c1-aef1-48ae-8eb4-0bcf124e567d.cxg/
Fetal Tissue Atlas	Suo *et al.*, 2022	Array Express:E-MTAB-11343
Thymus Atlas	Park *et al.*, 2020	Array Express: E-MTAB-8581
CD34 in vitro cultures	Ulezko Antonova *et al.*, 2023	GEO: GSE247692
CTICA	Dominguez Conde *et al.*, 2022	Array Express: E-MTAB-11536
BPDCN	Griffin *et al.*, 2023	GEO: GSE227690
Mouse BM and spleen	Rodrigues *et al.*, 2018	GEO: GSE114315